

RELATIVISTIC CHARGED PARTICLE IDENTIFICATION BY ENERGY LOSS

✖ 5618

W. W. M. Allison

Nuclear Physics Laboratory, University of Oxford, Oxford, United Kingdom OX1
 3RH

*J. H. Cobb**

Department of Physics, University of Lancaster, Lancaster, United Kingdom

CONTENTS

1	INTRODUCTION	254
1.1	<i>Relativistic Particle Identification</i>	254
1.2	<i>The Energy-Loss Method</i>	256
2	THE ATOMIC CROSS SECTION	260
2.1	<i>Kinematics</i>	260
2.2	<i>The Mean Energy Loss in a Medium</i>	263
2.3	<i>The Generalized Oscillator Strength Density</i>	265
2.4	<i>The Cross Section</i>	269
2.5	<i>A Calculation for Argon and the "Ideal" Detector</i>	271
3	THE ENERGY-LOSS DISTRIBUTION	275
3.1	<i>Calculation of the Energy-Loss Distribution</i>	275
3.2	<i>The Ionization Distribution</i>	277
3.3	<i>Comparison with Data</i>	279
4	MULTIPLE SAMPLING DETECTORS	283
4.1	<i>Statistical Analysis of Signals</i>	283
4.2	<i>The Choice of Detector Parameters</i>	286
4.3	<i>Practical Considerations</i>	290
4.4	<i>Existing Detectors</i>	293
5	SUMMARY	295
	<i>Acknowledgements</i>	295
	<i>Appendix: A picture of the field of a relativistic charged particle in a medium</i>	296

* Current address: EP Division, CERN, 1211 Geneva 23, Switzerland.

1 INTRODUCTION

1.1 *Relativistic Particle Identification*

Although the physical mechanisms underlying the phenomenon of energy loss by a fast charged particle passing through matter have been understood for many years (Bohr 1913, Bethe 1930), only recently has it become technically feasible to use energy-loss measurements for the identification of single particles in the relativistic region. Energy-loss measurements can provide single particle identification in the velocity range $5 \lesssim \beta\gamma \lesssim 300^1$ and therefore the technique is applicable both at fixed-target accelerators and at storage rings where interactions produce a high multiplicity of secondary particles with momenta of a few tens of GeV/c. The more conventional methods of particle identification by time-of-flight measurement and Cerenkov detectors fail or become difficult to use in this region, especially when implemented over a large solid angle. Inability to identify the secondary particles prohibits a complete analysis of an interaction; Lorentz invariant quantities cannot be constructed, the production and exchange of quantum numbers cannot be studied, and the analysis can only be performed in terms of laboratory variables.

The secondary particles to be identified are the leptons (electron and muon) and the long-lived stable hadrons (π meson, K meson, and proton), although the improbable but interesting observation of free fractionally charged quarks should not be overlooked. Specific methods exist for the identification of the leptons: muons, which are not greatly different in mass from pions, can be identified by their ability to penetrate great thicknesses of matter without interacting strongly; electrons, since their mass is so small, can be identified by their ability to initiate electromagnetic showers in a high- Z material. Hadrons must be identified by mass separation: a precision measurement of momentum in a magnetic spectrometer combined with an estimate of velocity yields the mass via the relation $\beta\gamma = P/\mu c$. The separation between particle species that can be achieved depends on the precision with which $\beta\gamma$ is estimated.

The particle velocity, β , may be deduced directly by measuring the time of flight over a fixed path of length L , the time difference between two species of masses μ_1 and μ_2 being $t_1 - t_2 \sim (L/2c) \times (\mu_1^2 - \mu_2^2)c^2/P^2$. If we assume a time resolution of a fraction of a nanosecond, then a path length of roughly P^2 meters is required to separate π and K mesons at a momentum of P GeV/c. This technique clearly becomes impractical when typical momenta

¹ Here β is the velocity, v/c , of the particle; γ is the Lorentz factor, $(1 - \beta^2)^{-1/2}$. The product $\beta\gamma$ is equal to $P/\mu c$, where μ is the mass of the particle and P is its momentum. The symbol m in this paper will be used for the mass of the electron.

exceed a few GeV/c. Alternatively, a Cerenkov counter may be used. Cerenkov radiation is emitted when a particle of velocity βc moves through a medium of refractive index $[\varepsilon(\omega)]^{1/2}$, where $\varepsilon(\omega)$ is the dielectric constant. This is free radiation of frequency ω emitted at an angle $\theta = \arccos \beta^{-1}[\varepsilon(\omega)]^{-1/2}$ when β exceeds the threshold velocity $\beta_{\varepsilon} = [\varepsilon(\omega)]^{-1/2}$ (see appendix). The mean number of photons emitted per unit path length is $dN/dx = \alpha/c[1 - 1/\beta^2\varepsilon(\omega)]d\omega$ and rises rapidly from threshold to 90% of the asymptotic value when $\beta\gamma \sim 3\beta_{\varepsilon}\gamma_{\varepsilon}$. A Cerenkov counter therefore provides a threshold rather than a velocity measurement. Usually practical considerations limit the spectrum to the optical region and, in order to obtain a refractive index sufficiently close to unity over a large frequency range, the radiator medium must be a gas. The photon flux is low and the path-length in the radiator must be rather long, up to several meters; it increases quadratically with the desired threshold. Several independent Cerenkov counters are required in order to provide sufficient thresholds to cover the entire spectrum of interesting momenta. Furthermore, to handle high multiplicity events, each has to be subdivided into many cells with the consequent difficulties of separating the light emitted at finite angles by different particles. Cerenkov counters have been fully reviewed by Litt & Meunier (1973).

The transition radiation emitted in the x-ray region when a charged particle crosses a discontinuity in dielectric constant may be detected and used for velocity discrimination (Garibyan 1960, Harris et al 1973, Allison 1977). This method is applicable only in the extreme relativistic region. With careful optimization a threshold of $\beta\gamma$ as low as 300–500 may be reached (Cobb et al 1977, Camps et al 1975, Commichau et al 1979). Relatively compact detectors can therefore be built to provide electron identification for momenta above 500 MeV/c and π meson identification above 50 GeV/c but there seems to be little practical possibility of achieving lower thresholds.

There is therefore a region where it is difficult to use the more conventional methods of particle identification. Recent attention has turned to the use of ionization measurements.

By ionization measurements we mean an indirect estimate of the energy loss, Δ , of a charged particle as it passes through a thin absorber, specifically by measuring the number of electrons liberated in a gas-filled proportional counter. The energy loss of a charged particle rises with $\beta\gamma$ and a measurement of it may be used to estimate the velocity. This proportional counter can be the same device that provides the spatial coordinates for momentum measurement and pattern recognition, so that particle identification will be available over the entire solid angle covered by the detector.

The use of energy-loss measurements for the identification of relativistic

particles was first discussed in detail by Alikhanov et al (1956). Measurements of ionization are commonly made in nuclear emulsions and in bubble chambers for the identification of nonrelativistic particles. With recent technical developments of proportional counters, the method can be extended to the relativistic region; several large ionization detectors are currently operating or under construction (see Table 2). Nevertheless the required mass resolution is not easily achieved because of the weak dependence of the ionization on velocity and the intrinsic statistical fluctuations of the ionization process. Therefore, to optimize the performance of such detectors, the underlying physics has to be understood. This review discusses the physics of ionization by a relativistic charged particle and how this is related to the mass resolution of a possible detector.

1.2 The Energy-Loss Method

The energy-loss or ionization method complements Cerenkov counters and x-ray transition radiation detectors by using the broad spectral range of virtual photons associated with the incident charged particle, from the soft ultraviolet to the x-ray region, with the atoms of the absorber medium acting as detectors. The large bandwidth and indirect means of observation of these photons lead to the large ("Landau") fluctuations in the signals from a proportional counter. Figure 1 shows the spectrum of signals observed when protons of $\beta\gamma = 3$ pass through a 2.3-cm thick proportional counter filled with argon at atmospheric pressure (Walenta et al 1979). The data for electrons with $\beta\gamma = 4000$ show a similar spectrum with the peak shifted upwards by $\sim 50\%$. The spectrum describes indirectly the probability $F(\Delta)$ of an energy loss Δ when the particle passes through the counter. Each Δ is the sum of energy transfers E_i in 50–100 distinct collisions between the particle and the gas atoms. The observation is indirect because what is measured is the number of ionization electrons in the gas rather than the energy loss itself. The collisions include the excitation of bound and unbound atomic states and "hard" scatters between the charged particle and quasi-free atomic electrons. The spectrum of energy transfers extends from a few eV up to the kinematic limit, $E_{\max} \sim 2m\beta^2c^2\gamma^2$, for a collision between a heavy charged particle and a free electron of mass m . The cross section for these hard collisions is described by the familiar Rutherford formula, $d\sigma/dE \sim 1/(\beta^2E^2)$, and consequently changes insignificantly with $\beta\gamma$ in the relativistic region ($\beta\gamma \gtrsim 4$). From the point of view of particle identification these hard collisions are a nuisance for they contribute to the "tail" extending to high energies (Figure 1). Individual collisions hard enough to eject a relativistic electron are rare and well beyond the dynamic range of typical ionization measurements. For

this reason we may restrict the discussion to nonrelativistic electrons. A fortiori the energy transfer is negligible compared with the incident particle energy. The peak region of the distribution is largely the result of soft collisions in which the atom as a whole absorbs a virtual photon, producing ionization. The energies involved in such collisions are characterized by the atomic structure of the material and the cross-section peaks in the region of the photoabsorption edges.

As discussed in the appendix, the electromagnetic field of a moving charged particle can be described as expanding in the transverse dimension as the velocity approaches the phase velocity of light in the medium, and the energy-loss cross section grows logarithmically with the $\beta\gamma$ of the particle. The peak of the energy-loss spectrum, or any other estimator of the soft collisions, therefore rises with $\log \beta\gamma$. This dependence of the ionization on velocity enables us to estimate the particle mass in the relativistic region. The rise would continue indefinitely in a medium of zero density. In a medium of finite density the dielectric properties modify the electromagnetic field limiting its expansion (Fermi 1940, Crispin & Fowler 1970). At

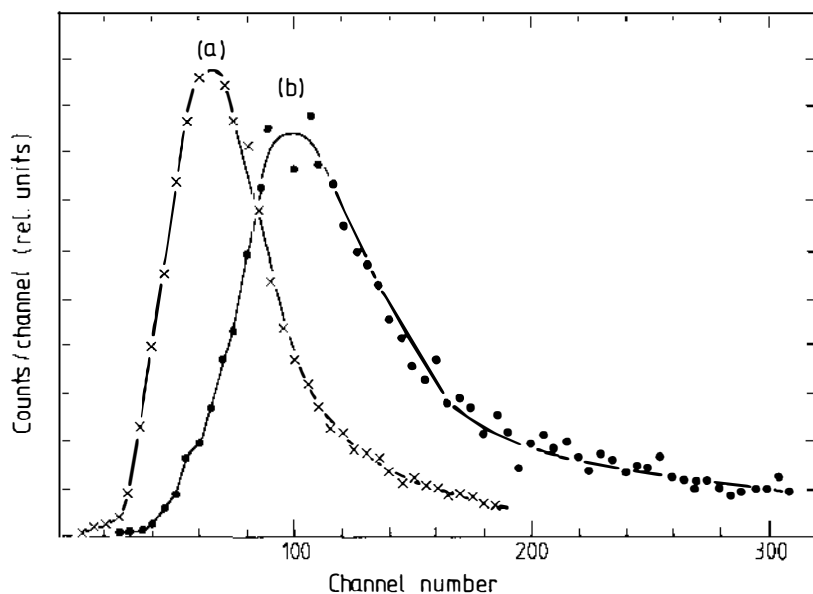


Figure 1 The observed ionization pulse height distributions in 2.3 cm of argon/10% CH₄ at 1 atm for (a) protons 3 GeV/c and (b) electrons 2 GeV/c (Walenta et al 1979). The peaks of the distributions correspond to an energy loss of about 4 keV. The lines are drawn simply to guide the eye.

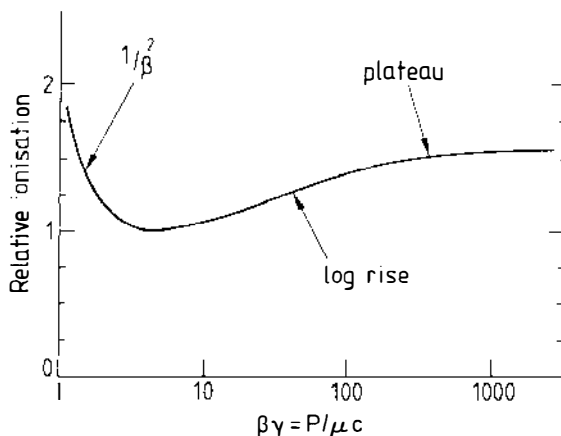


Figure 2 The typical dependence of ionization on $\beta\gamma$.

large values of $\beta\gamma$ the peak energy loss becomes independent of velocity². The dependence of the energy loss on $\beta\gamma$ is shown schematically in Figure 2. The nonrelativistic region where the energy loss falls as $1/\beta^2$ is well known. The region of the “relativistic rise” starts at $\beta\gamma \sim 4$ and the energy loss rises logarithmically with $\beta\gamma$ until the Fermi plateau is reached. The magnitude of the relativistic rise depends upon the atomic structure and density of the material. It is a few percent in solids and liquids and 50–70% in high- Z noble gases at atmospheric pressure, reaching the plateau for $\beta\gamma \sim 200$ –500. A gas is therefore the only practical choice for the sampling medium of an ionization detector.

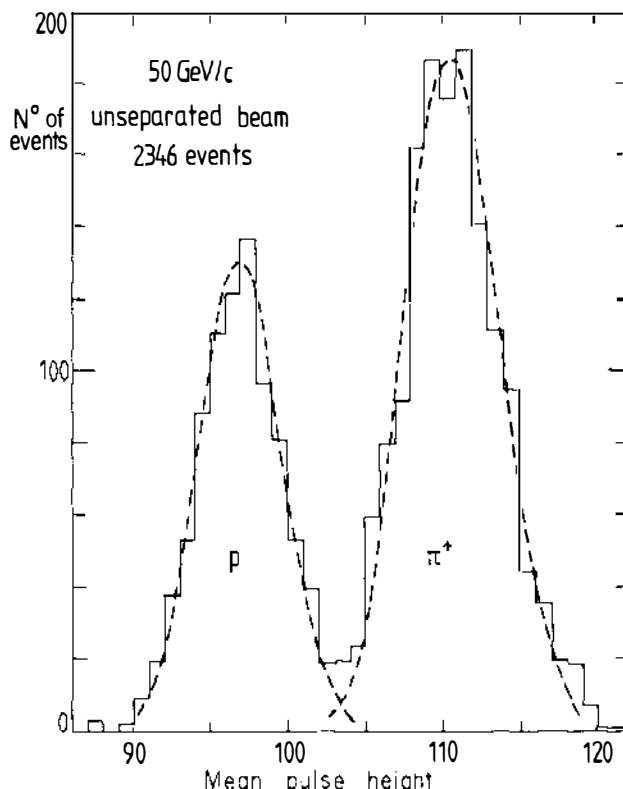
Many independent measurements or samples of ionization are necessary to resolve K and π mesons of the same momentum. Typically the ionization must be measured to 5–6% (FWHM) by collecting a spectrum such as Figure 1a for *each track*. Because of the distribution tail, resolution is lost if, instead, a smaller number of thicker samples is used. Usually ionization detectors make 100–300 measurements of the energy loss of a single particle in a total thickness of 100–1000 cm atm. The single sample thickness is chosen to represent a statistically significant number of soft collisions but to keep the probability of a hard collision small. The information gained from the multiple sampling of the energy-loss distribution must then be analyzed carefully to obtain a normally distributed estimator of ionization with a resolution of a few percent. A common procedure is to take the mean of the

² This applies to any form of restricted energy loss; the true mean energy loss continues to rise even in the Fermi plateau region, simply through an extension of the upper kinematic limit. It is not, however, an experimentally accessible parameter.

lowest 40–60% of the measurements. Figure 3 (Lehraus et al 1978) shows an example of the mass resolution that may be achieved in this way.

In this review we show how the mass resolution of a detector may be calculated from the detector parameters and the atomic structure of the medium through the well-defined intermediate steps of the differential energy-loss cross section $d\sigma/dE$ and the energy-loss distribution in a finite material thickness $F(\Delta)$. The discussion therefore falls naturally into three sections.

In Section 2 we derive the relationship between $d\sigma/dE$ and the atomic inelastic structure function $f(k, \omega)$. The latter, more generally known as the generalized oscillator strength density, may be modeled using the experimental photoabsorption cross section of the medium, $\sigma_v(E)$. Knowing $d\sigma/dE$, including its velocity dependence, we may calculate the mass resolution for particles of known momentum incident on an ideal detector in which data on every collision that occurs are available for analysis. Such detectors are not realizable; practical detectors have a coarse grain structure and measure $F(\Delta)$ rather than $d\sigma/dE$.



In Section 3 we discuss how $d\sigma/dE$ may be folded to give $F(\Delta)$. We comment on the empirical relationship between $F(\Delta)$ and the observed ionization distribution and finally compare experimental data with theoretical predictions.

In Section 4 we show how data from practical devices may be analyzed and how the ionization and the mass resolution depend on the detector parameters and the choice of gas. We develop some simple formulae that, with some qualifications, describe the resolution of a range of devices. We mention some of the practical difficulties that are encountered in the design of such devices and summarize the properties of existing detectors.

2 THE ATOMIC CROSS SECTION

2.1 Kinematics

As it passes through a medium, a fast charged particle loses energy in a number of independent collisions each with its own energy and momentum transfer (E, \mathbf{p}) from the particle to the medium³. The number of such collisions follows a Poisson distribution with mean given by $N_a \sigma_a x$, where N_a is the number of atoms per unit volume, σ_a is the atomic cross section, and x the thickness of the medium. The distribution of the energy loss Δ in x due to all these collisions (the energy loss distribution) is therefore completely defined once the cross section is known as a function of E and \mathbf{p} .

The first constraint on a collision comes from the fact that the incident fast particle (velocity βc and mass μ) is not excited by the collision. This reduces to

$$E(1 - E/2\gamma\mu c^2) = \beta \cdot \mathbf{p} c - p^2/2\gamma\mu. \quad 1.$$

For reasons explained in the introduction we are only concerned with soft collisions ($E \ll \gamma\mu c^2$, $p \ll \beta\gamma\mu c$) for which Equation 1 simplifies to

$$E = \beta p c \cos \psi. \quad 2.$$

We therefore consider the cross section as a function of E and the modulus $|\mathbf{p}|$. Figure 4 shows the E vs $|\mathbf{p}|$ plane with lines of constant ψ , which is the angle between \mathbf{p} and β . Since we are concerned with energy-loss processes, E as defined above is positive and ψ lies in the first quadrant. The limit $\psi = 0$ gives for an energy E a minimum momentum transfer equal to $E/\beta c$. The boundary of the physical scattering region is therefore a function of β , and Figures 4 and 5 show this for $\beta = 0.9$. If E , p , and ψ are measured for a single

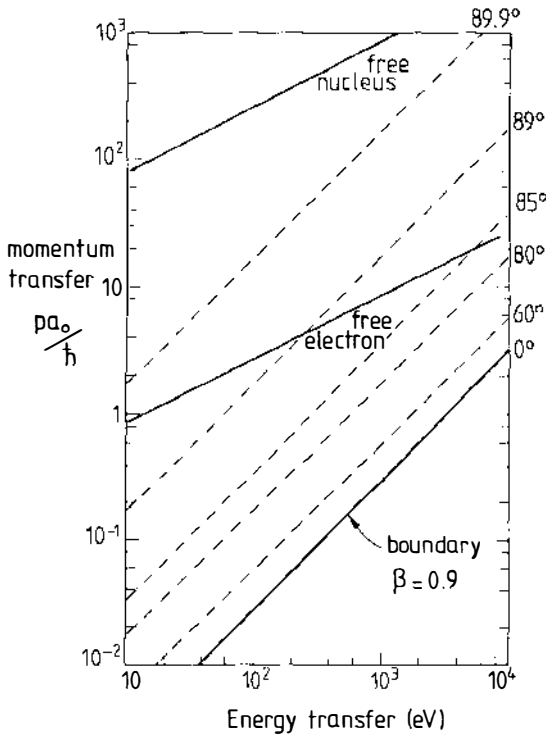


Figure 4 The kinematic region for soft energy and momentum transfer in natural units (a_0 = Bohr radius) for $\beta = 0.9$. Dashed lines indicate the recoil angle ψ . Elastic collisions with a free stationary electron or nucleus ($A = 4$) follow the solid lines.

energy-loss “collision,” Equation 2 shows that β may be determined⁴. Normally data on energy loss contain no information on p or ψ ; we must integrate the cross section over these variables.

Further information on the cross section in the (E, p) plane requires some knowledge of the target medium. Consider collisions with a single isolated electron or nucleus. For a free stationary electron the constraint is $E = p^2/2m$. This line and an equivalent line for typical nuclear collisions ($A = 4$) are shown on Figure 4. Nuclear collisions contribute negligibly to the energy-loss process even for large values of momentum transfer (small impact parameter). Such collisions are important in giving rise to multiple scattering. We may ignore radiative nuclear collisions (Bremsstrahlung) as exceptional processes in absorbers whose thickness is 10^{-3} or less of a

⁴ This is the principle of the “ring imaging” Cerenkov counter (Seguinot & Ypsilantis 1977). However, being sensitive only to β , the method loses resolution at high values of $\beta\gamma$.

radiation length. We conclude that the dominant inelastic process in the collision of fast particles with atoms will be quasi-elastic collisions with constituent electrons.

Consider now a medium containing *bound* electrons with binding energy E_1 and internal momentum \mathbf{q} . Typically \mathbf{q} is of order $(2mE_1)^{1/2}$. Kinematics of the electron requires $E = E_1 + (\mathbf{p} + \mathbf{q})^2/2m$. This traces out a broad band on the (E, p) plane according to the magnitude and direction of \mathbf{q} . The band consists of two parts: the resonance region where $p^2/2m$ is small compared with E_1 , and the quasi-free region where the constituent electron behaves almost as if it were free and stationary (Rutherford scattering). This is illustrated in Figure 5 for the example of a single atomic shell of binding energy 30 eV. Our problem is to evaluate the cross section at each point on this plane; we expect that most of the cross section lies within such bands.

Since the interaction involves the exchange of a virtual photon, the range and, therefore, the cross section increase as the photon becomes more nearly real. Figure 5 shows the relation between E and p for real photons in the absence of dispersion ($p = E/c$). This line lies just outside the physical

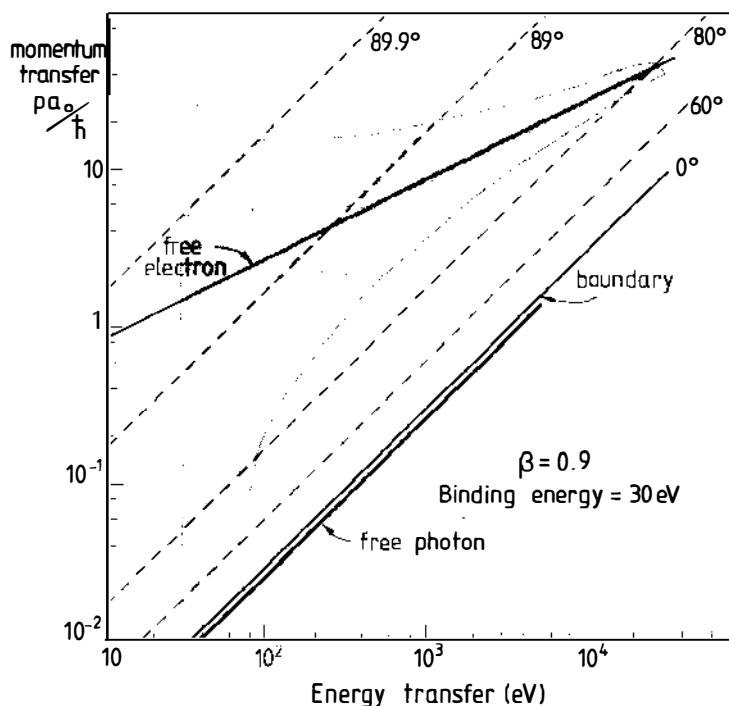


Figure 5 The kinematic region as described in Figure 4. The shading describes qualitatively the region for collisions with a bound electron, binding energy 30 eV. The energy-momentum relation for the absorption of free photons in the low density limit ($\epsilon = 1$) is also shown.

region for energy-loss collisions. As β tends to one, this boundary of the physical region asymptotically approaches the real photon condition giving the cross section increase. Note that all the increase comes at very low p in the resonance region. At finite densities the photon condition is given by $p = E\epsilon^{1/2}/c$ and the asymptotic behavior is modified. If ϵ , the dielectric constant, is greater than one, the physical region may cross the photon line and Cerenkov radiation results; if ϵ is less than one, the increase of the cross section with β saturates since the physical region never reaches the photon line (see appendix).

We write the complex dielectric constant of a medium, $\epsilon = \epsilon_1 + i\epsilon_2$, where ϵ_1 and ϵ_2 describe its polarization and absorptive properties respectively. Indeed the atomic photoabsorption cross section, σ_γ , is directly related to ϵ_2 and the electron density N by

$$\sigma_\gamma = \frac{Z\omega}{Nc} \frac{\epsilon_2}{(\epsilon_1)^{1/2}} \simeq \frac{Z\omega}{Nc} \epsilon_2, \quad 3.$$

where σ_γ and ϵ are functions of $\omega (= E/\hbar)$ and Z is the atomic number. The second form of Equation 3 applies for low density media ($\epsilon_1 \sim 1$): ϵ_1 is given in terms of ϵ_2 by the Kramers-Kronig relation (see, for example, Jackson 1975). Just as $\epsilon(\omega)$ comprises all the necessary knowledge of the medium in the restricted kinematic region for free photons, we may introduce $\epsilon(k, \omega)$, the generalized dielectric constant ($k = p/\hbar$), to describe the response of the medium over the whole scattering region for inelastic collisions. The energy-loss cross section may be derived in terms of $\epsilon(k, \omega)$ and in turn $\epsilon(k, \omega)$ may be related to atomic matrix elements.

For free photons the difference between a perfectly homogeneous medium and an inhomogeneous medium of the same mean density gives rise to the incoherent scattering away from the forward direction known as Rayleigh scattering. For the virtual photons associated with an incident charged particle, scattering from inhomogeneities in the dielectric gives rise to transition radiation (Garibyan 1960). In fact, such scattering only occurs from macroscopic inhomogeneities even at x-ray wavelengths. We may therefore ignore the effect of inhomogeneities in the medium and work with a continuum model.

2.2 The Mean Energy Loss in a Medium⁵

For collisions in which E is very small compared with the incident particle energy, we may calculate the cross section treating the electromagnetic field semiclassically. We derive the electric field \mathbf{E} at the position of the particle, $\mathbf{r} = \boldsymbol{\beta}ct$, and describe the mean energy loss per unit time as the effect of this

⁵ The reader who is not concerned with the details of the cross-section derivation may wish to skip Sections 2.2 and 2.3.

electric field doing work on the particle. In Section 4 we reinterpret this energy loss as a probability of loss of discrete energy $\hbar\omega$ in each frequency range; this is the quantization method originally introduced by Planck to describe black body radiation and generally known as semiclassical radiation theory. In this approach the density effect is included from the beginning rather than treated as a correction (Sternheimer 1952). This is appropriate because the effect is significant for particle identification. Derivations that overlap in part with the next two sections were given by Landau & Lifshitz (1960) and in the major review of energy loss by Fano (1963).

In a nonmagnetic dielectric medium Maxwell's equations may be written (using Gaussian units)

$$\operatorname{div} \mathbf{H} = 0; \quad \operatorname{curl} \mathbf{E} = -\frac{1}{c} \frac{\partial \mathbf{H}}{\partial t} \quad 4.$$

$$\operatorname{div} (\epsilon \mathbf{E}) = 4\pi\rho; \quad \operatorname{curl} \mathbf{H} = \frac{1}{c} \frac{\partial (\epsilon \mathbf{E})}{\partial t} + \frac{4\pi}{c} \mathbf{j}. \quad 5.$$

The incident charge velocity βc gives the driving terms;

$$\rho = e\delta^3(\mathbf{r} - \beta c t); \quad \mathbf{j} = \beta c \rho. \quad 6.$$

We analyze the problem in terms of potentials in the Coulomb gauge;

$$\mathbf{H} = \operatorname{curl} \mathbf{A}; \quad \operatorname{div} \mathbf{A} = 0; \quad \mathbf{E} = -\frac{1}{c} \frac{\partial \mathbf{A}}{\partial t} - \operatorname{grad} \phi. \quad 7.$$

Equations 4 are satisfied identically. Equations 5 become

$$\begin{aligned} \nabla \cdot (\epsilon \nabla \phi) &= -4\pi e \delta^3(\mathbf{r} - \beta c t); \\ -\nabla^2 \mathbf{A} &= -\frac{1}{c^2} \frac{\partial}{\partial t} \left(\epsilon \frac{\partial \mathbf{A}}{\partial t} \right) - \frac{1}{c} \frac{\partial}{\partial t} (\epsilon \nabla \phi) + 4\pi e \beta \delta^3(\mathbf{r} - \beta c t). \end{aligned} \quad 8.$$

These equations are solved by expressing all fields in terms of their Fourier transforms;

$$\mathbf{F}(\mathbf{r}, t) = \frac{1}{(2\pi)^2} \int d^3k \, d\omega \, \mathbf{F}(\mathbf{k}, \omega) \exp i(\mathbf{k} \cdot \mathbf{r} - \omega t). \quad 9.$$

One obtains

$$\begin{aligned} \phi(\mathbf{k}, \omega) &= 2e\delta(\omega - \mathbf{k} \cdot \beta c)/k^2\epsilon; \\ \mathbf{A}(\mathbf{k}, \omega) &= 2e \frac{(\omega \mathbf{k}/k^2 c - \beta)}{(-k^2 + \epsilon \omega^2/c^2)} \delta(\omega - \mathbf{k} \cdot \beta c). \end{aligned} \quad 10.$$

The electric field in space and time may then be expressed as follows

$$\mathbf{E}(\mathbf{r}, t) = (1/2\pi)^2 \int \int [i\omega/c \mathbf{A}(\mathbf{k}, \omega) - i\mathbf{k}\phi(\mathbf{k}, \omega)] \exp i(\mathbf{k} \cdot \mathbf{r} - \omega t) d^3k d\omega \quad 11.$$

The mean energy loss per unit length, known conventionally as $\langle dE/dx \rangle$, is due to the longitudinal component of \mathbf{E} at the point $\mathbf{r} = \beta c t$:

$$\langle dE/dx \rangle = \frac{e\mathbf{E}(\beta ct, t) \cdot \boldsymbol{\beta}}{\beta} \quad 12.$$

$$\begin{aligned} \langle dE/dx \rangle &= \frac{e^2 i}{\beta^2 \pi^2} \int \int \left[\frac{\omega \mathbf{k} \cdot \boldsymbol{\beta}}{c} \left(\frac{\omega \mathbf{k} \cdot \boldsymbol{\beta}}{k^2} - \beta^2 \right) \right] \left(-k^2 + \frac{\varepsilon \omega^2}{c^2} \right) - \frac{\mathbf{k} \cdot \boldsymbol{\beta}}{k^2 \varepsilon} \Big] \\ &\times \delta(\omega - \mathbf{k} \cdot \boldsymbol{\beta} c) \exp i(\mathbf{k} \cdot \boldsymbol{\beta} c - \omega) t d^3k d\omega \end{aligned} \quad 13.$$

$$\begin{aligned} &= \frac{e^2 i}{\beta \pi} \int d\mathbf{k} \int_{-\infty}^{\infty} d\omega \frac{k}{\beta} \\ &\times \left[\omega \left(\frac{\omega^2}{k^2 c^2} - \beta^2 \right) \right] \left(-k^2 c^2 + \varepsilon \omega^2 \right) - \frac{\omega}{k^2 \varepsilon c^2} \Big]. \end{aligned} \quad 14.$$

In the last step we have re-expressed the d^3k integration as $2\pi k^2 dk d(\cos \psi)$ and integrated over $\cos \psi$. In doing so we have assumed that ε is isotropic. Note that the time dependence has dropped out but that the integration is still over both positive and negative ω . Since $\varepsilon(-\omega) = \varepsilon^*(\omega)$ we may combine positive and negative frequencies:

$$\begin{aligned} \langle dE/dx \rangle &= -\frac{2e^2}{\beta^2 \pi} \int_0^{\infty} d\omega \int_{\omega/v}^{\infty} dk \\ &\times \left[\omega k (\beta^2 - \omega^2/k^2 c^2) \operatorname{Im} \left(\frac{1}{-k^2 c^2 + \varepsilon \omega^2} \right) - \frac{\omega}{k c^2} \operatorname{Im} \left(\frac{1}{\varepsilon} \right) \right], \end{aligned} \quad 15.$$

where the integration is now over the physical scattering region of Figure 5 with $E = \hbar\omega$ and $p = \hbar k$. The upper limits of integration written formally as infinity will not concern us in our study of thin absorbers.

2.3 The Generalized Oscillator Strength Density

The only unknown quantity in Equation 15 is the complex dielectric constant, which is a function of k as well as of ω , as discussed at the end of Section 2.1. It is convenient to express the imaginary part, ε_2 , in terms of the generalized oscillator strength density $f(k, \omega)$ thus

$$\varepsilon_2(k, \omega) = \frac{2\pi^2 N e^2}{m\omega} f(k, \omega). \quad 16.$$

Fano & Cooper (1968) reviewed the importance of the concept of oscillator strength in atomic physics and its relation to the simple classical model. Its generalization as a function of k as well as of ω was discussed by Inokuti (1971). The function $f(k, \omega) d\omega$ is a measure of the fraction of electrons coupling to the field between ω and $\omega + d\omega$ when the wave number is k : $f(k, \omega)$ is related to the atomic matrix elements between the ground state and the complete set of orthogonal atomic states n with excitation $(E_n - E_0)$ as follows

$$f(k, \omega) = \frac{1}{Z} \sum_n \frac{2m(E_n - E_0)}{\hbar^2 k^2} \delta\left(\omega - \frac{E_n - E_0}{\hbar}\right) \left| \langle n | \sum_{j=1}^Z \exp(i\mathbf{k} \cdot \mathbf{r}_j) | 0 \rangle \right|^2. \quad 17.$$

The sum over n includes both discrete and continuum states.

For atomic hydrogen $f(k, \omega)$ may be calculated rigorously; such calculations were reviewed by Inokuti (1971). They show a resonance region and a quasi-free region as expected from our qualitative discussion based on constituent scattering (Figure 5). For other atoms reasonably reliable calculations by Hartree-Fock and other methods have been made (McGuire 1971, Manson 1972, Berg & Green 1973, Inokuti et al 1978). Experimental investigations of the energy and momentum transfer of low energy electrons in thin targets have been used to investigate $f(k, \omega)$ for many atoms and molecules (see, for example, Bonham et al 1978).

In the context of relativistic charged particle identification, it is not clear that the finer details of the atomic structure are significant. The energy loss measured in an experiment with, for example, a proportional chamber may be discussed adequately with a simplified model of the generalized oscillator strength density. Such a model may be constructed from the photoabsorption cross section using the dipole approximation in the resonance region and point-like scattering in the quasi-free region.

Where ka is small, the dipole approximation is valid (a is the size of the ground-state orbital). This means that the exponential in Equation 17 may be expanded, retaining only the term linear in k . Then the only states that contribute to the sum over n are those that correspond to optically "allowed" transitions, and $f(k, \omega)$ is independent of k . In this region, therefore, $\varepsilon_2(k, \omega)$ is independent of k and equal to its value for free photons. Outside the dipole region the generalized oscillator strength is still constrained by the Bethe sum rule (Bethe 1930, Bethe & Jackiw 1968):

$$\int_0^\infty f(k, \omega) d\omega = 1. \quad 18.$$

This sum rule⁶ says that the area under every slice of the $f(k, \omega)$ surface at constant k is unity⁷—in fact, if $f(k, \omega) d\omega$ represents the fraction of electrons coupling to the field in the range ω to $\omega + d\omega$, f should integrate to unity. This result is quite general and goes beyond the dipole approximation. At high k many of the contributing atomic states have nonvanishing higher multipole matrix elements and are different from those contributing in the dipole-dominated low- k region.

We can now make a model of $f(k, \omega)$. We assume that we may extend the dipole approximation to describe the entire resonance region, defined as the area below and to the right of the free electron line in Figure 5. Thus in this region, $f(k, \omega)$ is independent of k and given in terms of the atomic photoabsorption cross section of free photons, $\sigma_\gamma(\omega)$ by Equations 3 and 16:

$$f(k, \omega) = \frac{mc}{2\pi^2 e^2 Z} [\sigma_\gamma(\omega)]. \quad 19.$$

The quantity $\sigma_\gamma(\omega)$ is a convenient experimentally available measure of oscillator strength density. At fixed k we therefore have a total oscillator strength in the resonance region given by

$$\int_{\text{res}} f(k, \omega) d\omega = \frac{mc}{2\pi^2 e^2 Z} \int_{\hbar k^2/2m}^{\infty} [\sigma_\gamma(\omega)] d\omega. \quad 20.$$

The remaining oscillator strength necessary to satisfy the Bethe sum rule must be attributed to the quasi-free region. We approximate this by a δ function on the free electron line, ignoring the Fermi motion of bound electrons:

$$f(k, \omega) = \frac{mc}{2\pi^2 e^2 Z} \delta\left(\omega - \frac{\hbar k^2}{2m}\right) \int_0^\omega \sigma_\gamma(\omega') d\omega'. \quad 21.$$

The normalization is determined uniquely by the Bethe sum rule. The integral in Equation 21 describes the number of electrons that are effectively free for an energy transfer, $\hbar\omega$. We note that the photoabsorption cross section satisfies the Thomas-Reiche-Kuhn sum rule,

$$\int_0^\infty \sigma_\gamma(\omega) d\omega = 2\pi^2 e^2 Z/mc. \quad 22.$$

⁶ In a relativistic theory the sum rule applies at constant $q^2 = k^2 - \omega^2/c^2$. On or near the free electron line where we make use of the Bethe sum rule $\omega \ll kc$ and the nonrelativistic form (Equation 18) is a good approximation.

⁷ This normalization follows from the choice of N as the electron density adhered to throughout this paper. This is convenient for handling gas mixtures.

This model may be written formally as the following general expression for $\varepsilon_2(k, \omega)$:

$$\varepsilon_2(k, \omega) = \frac{Nc}{\omega Z} \left[\sigma_\gamma(\omega) H\left(\omega - \frac{\hbar k^2}{2m}\right) + \int_0^\omega \sigma_\gamma(\omega') d\omega' \delta\left(\omega - \frac{\hbar k^2}{2m}\right) \right], \quad 23.$$

where $H(x)$ is the step function, $H = 1$ for $x > 0$ and $H = 0$ otherwise. The approximation of the oscillator strength in the quasi-free region by a δ function is adequate since we are really only concerned with the projection of the cross section on the ω or energy transfer axis. Detailed calculations for argon, for example, (see Section 2.5) show that the contribution of the quasi-free region to the energy-loss process is very smooth, broad, and not large, even assuming the δ -function form (see Figure 6b).

Before we can integrate over k in Equation 15 we need $\varepsilon_1(k, \omega)$. The first term of Equation 15 contains a denominator $-k^2 c^2 + \varepsilon \omega^2$, which represents the photon propagator and is therefore large only near the photon line—that is, at the lower part of the resonance region where the dipole approximation is good. So for this term we ignore quasi-free electron scattering and write

$$\varepsilon_2(k, \omega) = \frac{Nc}{\omega Z} \sigma_\gamma(\omega) = \varepsilon_2(\omega) \quad 24.$$

for all k . The real and imaginary parts of ε are related by the Kramers-Kronig relation,

$$\begin{aligned} \varepsilon_1(\omega) - 1 &= \frac{2}{\pi} P \int_0^\infty \frac{x \varepsilon_2(x)}{x^2 - \omega^2} dx \\ &= \frac{2}{\pi} \frac{Nc}{Z} P \int_0^\infty \frac{\sigma_\gamma(x)}{x^2 - \omega^2} dx, \end{aligned} \quad 25.$$

where P indicates that the principal value of the integral is to be taken. Therefore ε_1 is independent of k for the first term of Equation 15 while for the second term it may be assumed to be unity for low density media.

We are now in a position to integrate over k in Equation 15. After some straightforward manipulation we get

$$\begin{aligned} \langle dE/dx \rangle &= - \int_0^\infty d\omega \frac{e^2}{\beta^2 c^2 \pi} \left[\frac{Nc}{Z} \sigma_\gamma(\omega) \ln [(1 - \beta^2 \varepsilon_1)^2 + \beta^4 \varepsilon_2^2]^{1/2} \right. \\ &\quad \left. + \omega \left(\beta^2 - \frac{\varepsilon_1}{|\varepsilon|^2} \right) \Theta + \frac{Nc}{Z} \sigma_\gamma(\omega) \ln \left(\frac{2m\beta^2 c^2}{\hbar \omega} \right) \right. \\ &\quad \left. + \frac{1}{\omega} \int_0^\omega \frac{\sigma_\gamma(\omega')}{Z} d\omega' \right], \end{aligned} \quad 26.$$

where $\Theta = \arg(1 - \varepsilon_1 \beta^2 + i\varepsilon_2 \beta^2)$ and in terms 1, 3, and 4 we have dropped factors of $1/|\varepsilon|^2$, which are unimportant in low density media.

2.4 The Cross Section

We now reinterpret Equation 26 in terms of a number of discrete collisions with energy transfer $E = \hbar\omega$. With N as the number of electrons per unit volume, $d\sigma/dE$ the differential cross section per electron per unit energy loss, the average energy loss is given by

$$\left\langle \frac{dE}{dx} \right\rangle = - \int_0^\infty NE \frac{d\sigma}{dE} \hbar d\omega \quad 27.$$

$$\begin{aligned} \frac{d\sigma}{dE} = & \frac{\alpha}{\beta^2 \pi} \frac{\sigma_\gamma(E)}{EZ} \ln[(1 - \beta^2 \varepsilon_1)^2 + \beta^4 \varepsilon_2^2]^{-1/2} + \frac{\alpha}{\beta^2 \pi} \frac{1}{N\hbar c} \left(\beta^2 - \frac{\varepsilon_1}{|\varepsilon|^2} \right) \Theta \\ & + \frac{\alpha}{\beta^2 \pi} \frac{\sigma_\gamma(E)}{EZ} \ln \left(\frac{2mc^2 \beta^2}{E} \right) + \frac{\alpha}{\beta^2 \pi} \frac{1}{E^2} \int_0^E \frac{\sigma_\gamma(E')}{Z} dE', \end{aligned} \quad 28.$$

where α is the fine structure constant and ε_1 , ε_2 , and Θ are derived from σ_γ using Equations 25, 24, and following 26 respectively.

In making this substitution we have implicitly assumed single photon exchange (per collision). A similar assumption enters if the first-order Born approximation is used explicitly and is valid for incident velocities much greater than the electron orbital velocities.

The first two terms of Equation 28 are referred to as the transverse cross section. They come from the magnetic vector potential term (in the Coulomb gauge) for which the electric field is transverse to the direction of 3-momentum transfer, $\hbar\mathbf{k}$. Comparing the first term (with $\varepsilon_2 = 0$) with the simple model described in the appendix, we recognize the factor $\ln(\gamma'^2)$ responsible for the relativistic increase of the cross section as well as its saturation. In the limit that ε_2 vanishes, the second term describes the emission of Cerenkov radiation; Θ jumps from near 0 below Cerenkov threshold to almost π above:

$$N \left(\frac{d\sigma}{d\omega} \right)_\varepsilon = \frac{\alpha}{c} \left(1 - \frac{\varepsilon_1}{\beta^2 |\varepsilon|^2} \right) \simeq \frac{\alpha}{c} \sin^2 \theta_\varepsilon. \quad 29.$$

This is the familiar result for the Cerenkov flux in terms of the Cerenkov angle θ_ε . Above ionization threshold ε_2 does not vanish and it is impossible to distinguish this component of the cross section as responsible for Cerenkov radiation; indeed this term may be negative. Chechin et al (1972) used a cross section identical with Equation 28 except in the form of this term. Their derivation depends on certain assumptions about the transparency of the medium that were first made by Budini & Taffara (1956).

Their formula has recently been used in calculations of energy loss by Lapique & Puiz (1980).

The third and fourth terms of Equation 28 are known as the longitudinal cross section. They come from the electrostatic term in the Coulomb gauge, which has the electric field parallel to the momentum transfer. In the nonrelativistic theory they are the only terms. Their sole dependence on velocity is through the $1/\beta^2$ factor common to all terms and so they become effectively constant in the relativistic region. The third term comes from the resonance region while the fourth represents Rutherford scattering from those electrons that are quasi-free for an energy transfer E . For low density media the longitudinal cross section does not depend on either ε_1 or density. The transverse cross section does depend on density and in the limit of zero density becomes

$$\frac{d\sigma_T}{dE} = \frac{\alpha}{\beta^2\pi} \left[\frac{\sigma_\gamma(E)}{EZ} (\ln \gamma^2 - \beta^2) \right]. \quad 30.$$

This cross section increases linearly with $\ln \gamma$ without saturation due to the density effect.

It is instructive to consider the limit $\beta = 1$ of the cross section in Equation 28. Let us approximate the dielectric constant, $\varepsilon(\omega)$, in terms of the plasma frequency, $\omega_p^2 = 4\pi Ne^2/m$, thus

$$\varepsilon_1 - 1 = \omega_p^2 P \int_0^\infty \frac{f(\omega') d\omega'}{\omega'^2 - \omega^2} \simeq \frac{\omega_p'^2}{\omega^2}, \quad 31.$$

where ω_p' is the effective plasma frequency due to those electrons that are effectively free; $\omega_p'^2(\omega) = 4\pi Ne^2/m \times \int_0^\omega f(\omega') d\omega'$. The second equality in Equation 31 is valid for values of ω near which $f(\omega)$ is smoothly varying⁸. With this approximation and insofar as ε_2 is small compared with $(\varepsilon_1 - 1)$, the transverse cross section becomes

$$\frac{d\sigma_T}{dE} = \frac{\alpha}{\beta^2\pi} \frac{\sigma_\gamma(E)}{EZ} \left[\ln \left(\frac{\omega^2}{\omega_p'^2} \right) - 1 \right]. \quad 32.$$

Comparing this with Equation 30 we expect the cross section to saturate at a velocity of order $\gamma = \omega/\omega_p'$. This result shows that the relativistic rise extends over the widest range for gases (low ω_p) with high ionization potentials (large ω) and is the reason for the choice of a gas, and a noble gas in particular, as the working media in relativistic dE/dx detectors. The

⁸ This relation depends on the approximation that

$P \int_0^\infty f(\omega') \left[\left(\frac{\omega'}{\omega} \right)^2 - 1 \right]^{-1} d\omega'$ is equal to $\int_0^\omega f(\omega') d\omega'$.

approximation in Equation 31 is made here for the purpose of illustration. In practice, the full expression of Equation 28 may be used.

To use Equation 28 we need only know the photoabsorption cross section per electron (σ_{γ}/Z) for the medium of interest. With the advent of powerful sources of synchrotron radiation have come reliable experimental photoabsorption data. References have been listed by Way (1978). For the noble gases see West & Marr (1976) and West & Morton (1978). For simple molecular gases including hydrocarbons and CO_2 see Lee et al (1973, 1977). Theoretical calculations for the elements are in fair agreement and may also be used (McGuire 1968). For mixtures of gases the cross section per electron may be constructed by independent addition. Where data for molecular gases are not available, the cross section may be approximated by independent addition of the elements, although this will clearly be a poor guess for the outer electrons whose energies are affected by chemical binding. Although calculated energy-loss distributions are not too sensitive to the assumed photoabsorption spectrum, it is important to ensure that for each element or molecule the spectrum satisfies the sum rule (Equation 22) including the contribution of discrete absorption lines. In the absence of firm data the sum rule may be satisfied artificially by adding the necessary absorption below threshold to account for discrete excitation. With σ_{γ}/Z known, ε_2 and ε_1 follow from Equations 3 and 25 respectively. We call calculations using the full Equation 28 together with photoabsorption cross sections the photo absorption ionization (PAI) model.

2.5 A Calculation for Argon and the "Ideal" Detector

Using the PAI model we explore the dependence of the energy-loss cross section for argon on energy transfer E , velocity β , and gas pressure P . Complete and reliable data on σ_{γ} are available (West & Marr 1976). Figure 6a shows $E\sigma_{\gamma}$ plotted against E on a log scale. Equal areas under this curve represent equal contributions to the optical oscillator strength density. The K, L, and M shells are clearly visible although there are contributions at intermediate energies owing to correlation effects (Chang & Fano 1976). Figure 6b shows $E^2 d\sigma/dE$ evaluated according to Equation 28 for $\beta = 1$ in argon at normal density. Equal areas under the curve represent equal contributions to the energy loss. The contributions from the Rutherford term, the transverse term (shaded), and the longitudinal term in the resonance region respectively are shown above one another. 1% of the total energy loss due to collisions of less than 50 keV is in the form of Cerenkov radiation below ionization threshold. An important difference between the shapes of Figures 6a and b is due to the slowly rising Rutherford or quasi-free term that forms a background under the resonant structures.

In the relativistic region the transverse cross section increases with $\ln \gamma$

until limited by the density effect. The combined cross section (Equation 28) normalized to its value at $\beta\gamma = 4$ is shown as a function of $\beta\gamma$ for three different values of energy transfer E in Figure 7. For particle identification we are interested in the slope of the relativistic increase and at what value of $\beta\gamma$ it saturates. We see that both of these quantities vary with E . The value of

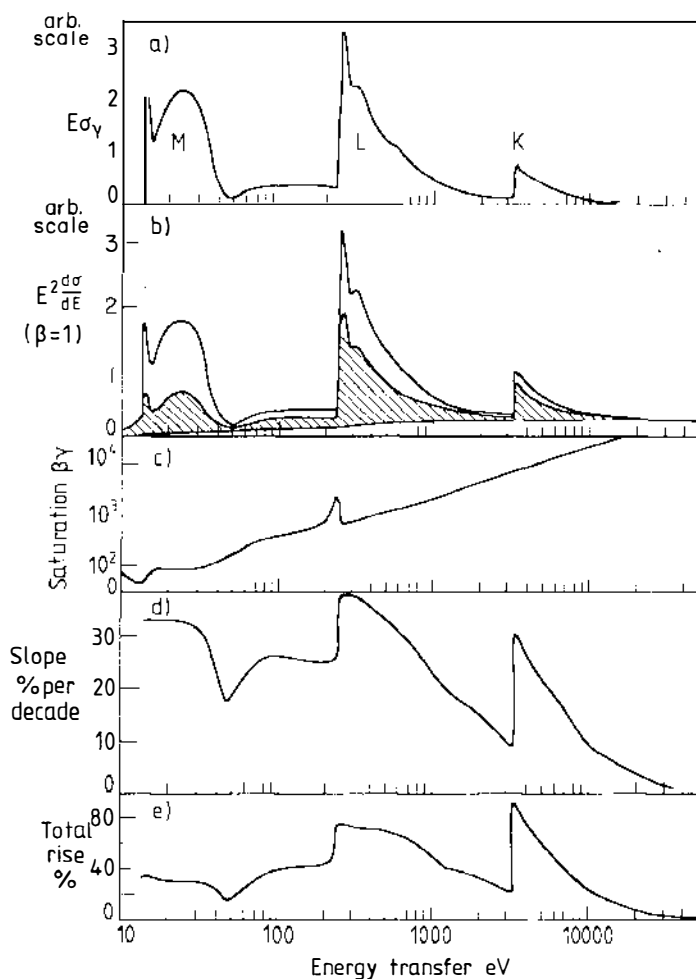


Figure 6 Results of a calculation based on the PAI model for argon at normal density as a function of energy transfer, E . (a) The input photoabsorption spectrum. (b) The calculated energy-loss cross section for $\beta = 1$. Upper unshaded area is the resonance region longitudinal term; shaded area is the transverse term; lower unshaded area is the quasi-free or Rutherford term. (c) The value of $\beta\gamma$ at which the slope of the log rise of the cross section for energy transfer E saturates (slope falls to 5% of maximum). (d) The slope of the log rise in the absence of density effect. (e) The total rise relative to minimum at normal density.

$\beta\gamma$ at which saturation is effectively complete is shown in Figure 6c. The behavior is very close indeed to a line $\beta\gamma = 2\omega/\omega_p'$ except at optical frequencies and just below the L-shell edge. This dependence was expected on the basis of Equation 32 and clearly gives a convenient way of estimating the saturation point. The density effect becomes significant at about 40% of this saturation value as shown in Figure 7. For the outer shell of electrons of argon this corresponds to $\beta\gamma \sim 40$ at normal density. As the density of argon is varied, the saturation point follows a (density) $^{-1/2}$ dependence.

The slope of the relativistic rise, which depends largely on the relative contribution of transverse and longitudinal terms, is shown as a function of E in Figure 6d. It is independent of density. The slope is given in percent per decade so that, for instance, the percentage difference in the cross section due to incident K and π mesons of the same momentum is half the figure shown. The total rise relative to the ionization minimum is shown in Figure 6e for argon at normal density.

In comparing the possible contribution made by different shells to particle identification we must consider statistical effects. There are about 30 collisions with M-shell electrons per centimeter of relativistic track in argon at normal density, between one and two collisions with L-shell electrons per centimeter, and one collision with a K-shell electron every 30 cm. This shows that, even in an "ideal" detector in which one could imagine recording every individual collision in the gas and its energy, K-shell ionization can make no effective contribution to individual particle identification. On the other hand, L-shell ionization is effective in a few meters, while in the absence of the density effect M-shell ionization would be effective in 15–20 cm.

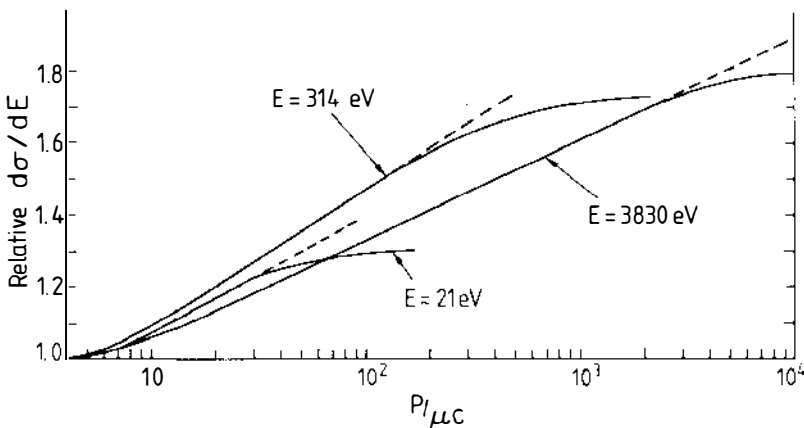


Figure 7 The calculated $\beta\gamma$ dependence of the energy-loss cross sections for three representative energies for argon at normal density normalized to $\beta\gamma = 4$. The dashed lines show the dependence in the low density limit.

In Figure 8 the solid curve shows the mass resolution obtainable from a knowledge of the spectrum of individual energy transfers of a particle with known momentum traversing one meter of pure argon at normal density. The resolution is calculated by a maximum likelihood analysis of this spectrum, using as likelihood the function $Nx(d\sigma/dE)$, which depends on $\ln(p/\mu)$. For this reason the resolution is expressed as the logarithm of the resolvable mass ratio. For example the K to π meson mass ratio represents a difference in $\ln \mu$ of 1.25. It is possible in principle to separate K and π mesons by the Rayleigh criterion (one FWHM) in the range $\beta\gamma = 4-150$ with such an "ideal" detector of length one meter. Whether this level of separation is sufficient depends on the circumstances of the experiment, in particular on the relative populations of the different masses and on the degree of confidence required. (In this illustrative discussion we have ignored the fact that K and π mesons of the same momentum have sufficiently different $\beta\gamma$ values that the resolution is not the same in the two cases). Alternatively we can consider the perfect "primary ionization" detector, which resolves the number of collisions without measuring their energies. Since such collisions are predominantly M-shell processes the

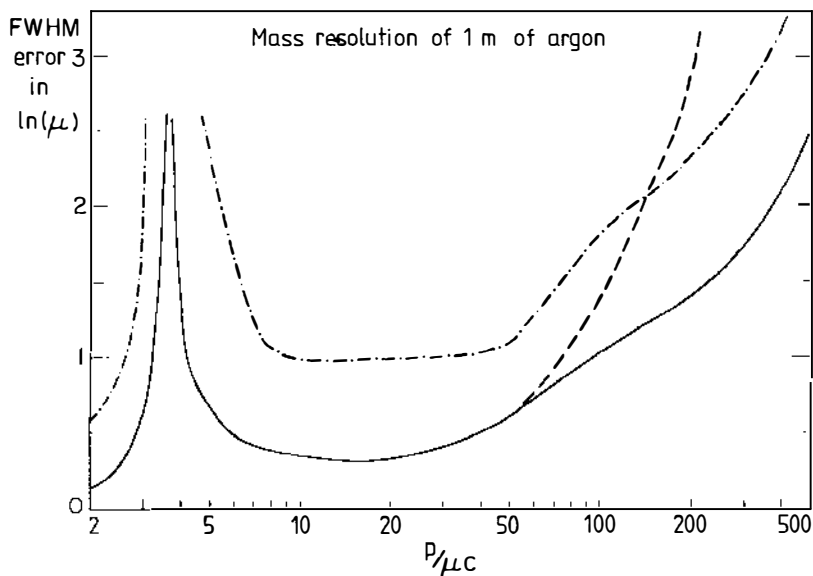


Figure 8 The potential and actual mass resolution inherent in the energy loss in 1 m of pure argon at normal density (excluding Cerenkov radiation below ionization threshold). Solid line: the energy transfer in every collision is known. Dashed line: only the number of such collisions is known (primary ionization). Dotted and dashed line: the integrated energy loss in each of 62×1.6 -cm samples is known (ISIS).

resolution is rapidly curtailed by the density effect above $\beta\gamma$ equal to 50. This is shown by the dashed line. At lower velocities all electron shells share in the log rise and $1/\beta^2$ behavior so that measurement of primary ionization is as effective as the ideal detector.

Neither of the above detectors is yet realizable. For comparison we show as a dash-dot curve the resolution of a practical device, ISIS1, described briefly in Section 4, which measures the energy loss integrated in each of 62×1.6 -cm samples. Its resolution is typically worse than ideal by a factor of two to three although the difference is much less pronounced at high $\beta\gamma$. This is because the sample length is of the order of the mean free path between L-shell collisions, which are the source of the rise in this region. At nonrelativistic velocities the mass resolution is excellent, simply on account of the steepness of the energy-loss curve (see Figure 2). Near $\beta\gamma = 3.5$ there is a "cross-over" region where particle identification is not possible (see, however, Footnote 13 in Section 4.1). We postpone further discussion on mass resolution to Section 4.

3 THE ENERGY-LOSS DISTRIBUTION

In Section 3.1 we consider how the cross section of Section 2 may be used to derive the energy-loss distribution in a finite thickness of material, and in Section 3.2 how to relate this to actual measurements. In Section 3.3 we compare the results of various calculations of energy loss with available data.

3.1 *Calculation of the Energy-Loss Distribution*

The probability distribution $F(x, \Delta)$ of energy loss Δ by particles of given velocity traversing a thickness of material x is uniquely determined by the cross section $d\sigma/dE$ and the number of electrons in the layer Nx . Since $d\sigma/dE$ has a significant value over a wide range of E , the distribution $F(x, \Delta)$ is both broad and skew. This problem was first described by Williams (1929) and recently was discussed fully by Bichsel & Saxon (1975). There are two approaches, the convolution method and the Laplace transform method.

The convolution method considers a very small thickness δx such that the chance of two collisions within δx is negligible. Then

$$F(\delta x, \Delta) = (1 - \tau) \delta(\Delta) + N\delta x \frac{d\sigma}{dE}(\Delta) + O(\tau^2), \quad 33.$$

where τ , the chance of one collision, is $N\delta x \int_0^\infty d\sigma/dE dE$. From this the distribution for any given thickness may be built up by repeated application

of the formula

$$F(2x, \Delta) = \int_0^{\Delta} F(x, \Delta - E) F(x, E) dE, \quad 34.$$

which follows from the statistical independence of the energy loss in different layers. Bichsel & Saxon (1975) used this method.

Alternatively the folding may be done by Monte Carlo method. The mean number of collisions, τ , in the sample is calculated from the integrated cross section. Then for each trial the actual number is chosen from a Poisson distribution with mean τ . Finally the energy loss is just the energy sum of such collisions chosen according to the normalized $d\sigma/dE$ spectrum. This or related methods have been used by Ispiryan et al (1974), Cobb et al (1976), and Ermilova et al (1977).

The Laplace transform method was introduced by Landau (1944). He considered the change in $F(x, \Delta)$ as a result of passing through a thin elemental layer δx :

$$\begin{aligned} F(x + \delta x, \Delta) - F(x, \Delta) = & -N\delta x \int_0^{\infty} \frac{d\sigma}{dE}(E) F(x, \Delta) dE \\ & + N\delta x \int_0^{\Delta} F(x, \Delta - E) \frac{d\sigma}{dE}(E) dE. \end{aligned} \quad 35.$$

The first term describes the probability that the energy loss was already equal to Δ before entering δx where a further collision increased the energy beyond Δ . The second term corresponds to the case in which the energy loss at x was $\Delta - E$ but a collision with energy E occurred in the element δx . This equation may be put in the form of a transport equation

$$\frac{\partial F}{\partial x}(x, \Delta) = \int_0^{\infty} N \frac{d\sigma}{dE}(E) [F(x, \Delta - E) - F(x, \Delta)] dE. \quad 36.$$

This may be solved by taking Laplace transforms of both sides with respect to Δ and solving for $\bar{F}(x, s)$, the transform of $F(x, \Delta)$:

$$\bar{F}(x, s) = \exp \left[-x \int_0^{\infty} N \frac{d\sigma}{dE}(E) (1 - e^{-sE}) dE \right] \quad 37.$$

where use has been made of the boundary condition:

$$F(x = 0, \Delta) = \delta(\Delta); \quad \bar{F}(x = 0, s) = 1. \quad 38.$$

Inverting the Laplace transform (σ is very small but positive)

$$F(x, \Delta) = \frac{1}{2\pi i} \int_{-i\infty + \sigma}^{i\infty + \sigma} ds \exp \left[s\Delta - x \int_0^{\infty} N \frac{d\sigma}{dE}(E) (1 - e^{-sE}) dE \right]. \quad 39.$$

This result is exact. On the other hand realistic models of the cross section are not simple and the integration must be carried out numerically. Talman (1979) recently used this method.

Of course, given the same cross section, $d\sigma/dE$, the convolution and Laplace transform methods must give the same energy-loss distributions. The important difference between the work of different authors has been the approximations made for $d\sigma/dE$ and the range of validity of the resulting energy-loss distributions, as discussed in Section 3.3. The convolution method is the easiest to handle for thin absorbers where the number of collisions is not large and acceptable approximations in the form of the cross section are few. For the new results reported in this paper we have used this method in conjunction with the PAI model.

3.2 *The Ionization Distribution*

Up to this point we have been discussing the distribution of energy loss in a thin absorber by a relativistic particle. Unfortunately this is not directly measurable⁹. The most faithful manifestation of the energy loss is the deposited ionization, but others, such as bubble density (Chechin et al 1972, Fisher et al 1975) and emulsion grain density (reviewed by Crispin & Fowler 1970), have been discussed. Except for the case of ionization these show poor velocity resolution and are not suitable for the identification of single particles. Therefore in the following we confine our attention to gas-filled proportional counters.

We assume that the number of electrons n_i liberated in the absorber is related to the energy deposited Δ by the relation

$$\Delta = n_i W \quad 40.$$

and that, on average, the energy per ion pair W is a constant independent of Δ . This assumption is essentially statistical and depends on the random nature of the secondary mechanisms responsible for thermalization of the deposited energy. The situation was discussed recently by Inokuti (1975). Experimental values of W vary from 26 eV for argon to 36 eV for nitrogen; for a review see ICRU (1979). For the energy deposited by relativistic charged particles, we are concerned with the linearity of Equation 40, not only for the combined energy loss Δ , but also at the level of individual energy transfers, E . Insofar as this is not so, the velocity dependence of ionization may not follow that of energy loss. Although this linearity must break down for E close to the first ionization potential, for mixtures involving molecular gases with low ionization potentials, departures from

⁹ By contrast the energy loss of low energy electrons is measured directly in the study of the generalized oscillator strength density (Bonham et al 1978).

linearity should be smaller than for pure noble gases. Photon data for an argon/methane mixture are consistent with constant W to within 3% at least above $E = 250$ eV. In propane W is constant to within 8% down to $E = 80$ eV (Srdoc 1973).

To calibrate absolutely an ionization distribution, the response to a known energy deposition must be measured. This usually takes the form of monochromatic x rays. However technical differences between x-ray and charged particle data, such as the effects of triggering or local saturation of the gas amplification, can make absolute calibration unreliable. Most data are uncalibrated or shown relative to other charged particle data at minimum ionization, $\beta\gamma \sim 4$.

While Equation 40 may apply statistically, for a fixed value of Δ there are fluctuations of n_i (Fano 1947). There are further statistical fluctuations in the gas amplification process of the n_i electrons at the collecting anode. This effect has been summarized by Charpak (1970) and the broad conclusion is that the rms of the combined fluctuations from both sources σ_p in the observed amplified signal P is

$$\sigma_p/P \sim n_i^{-1/2} \sim 0.17 \Delta^{-1/2} \quad 41.$$

where Δ is in keV. This relation is followed to within $\pm 10\%$ for photons in propane (Srdoc 1973). It represents the intrinsic energy resolution of a proportional counter. The fluctuations represented by Equation 41 are small compared to the fluctuations in the energy deposited itself. Consequently the intrinsic energy resolution is not an important parameter of an energy-loss detector.

Some of the energy loss may be carried away from the region of the track in the form of radiation. At intermediate energies the absorption length of the gas is too short but at x-ray energies fluorescent photons from K-shell vacancies may travel several centimeters. These are too rare to have an effect on the ionization loss distribution but may be useful for calibration purposes (Allison et al 1979). As far as the Cerenkov energy is concerned, we remark that all proportional chamber gas mixtures are chosen to have short ultraviolet photoabsorption lengths that prevent Geiger discharges in the gas amplification region. So that, while 1% of the energy loss may propagate away from the track in pure argon, in a practical proportional chamber gas the figure is smaller. The proportional chamber quenching gas with its low ionization potential also plays a major role converting metastable states into ionization. Without this mechanism the linear dependence of Equation 40 would be less plausible for collisions with outer electrons.

Energy is also carried away from the region of the track in the form of δ -ray electrons. Such electrons come from collisions of several tens of keV or

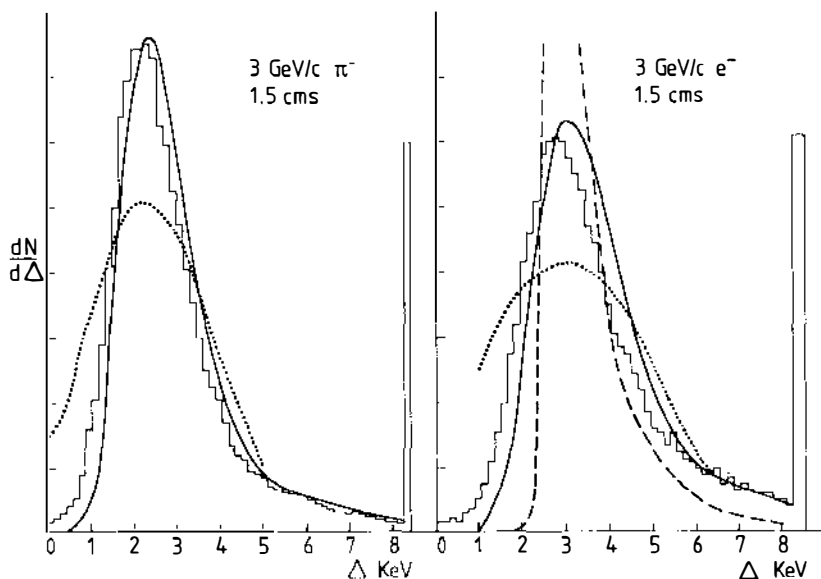


Figure 9 Experimental energy-loss distributions of Harris et al (1973) for π^- and e^- at 3 GeV/c in 1.5 cm of argon/7% CH_4 at normal density. The dashed and dotted curves are calculations using the model of Landau (1944) with corrections of Maccabee & Papworth (1969) and Blunck & Leisegang (1950) respectively. The solid curves are the predictions of the PAI model.

more and are in the tail of the energy-loss distribution. They are infrequent and their escape is not important.

3.3 Comparison with Data

The experimental data with which calculations may be compared consist of energy-loss distributions¹⁰ $F(\Delta)$ and their dependence on velocity, pressure, thickness, and composition. Rather few clean energy-loss distributions have appeared in the literature (Dimcovski et al 1971, Harris et al 1973, Kopot et al 1976, Bunch 1976, Walenta et al 1979, Allison et al 1979). However, there are many measurements of widths and peaks of distributions, for instance Jeanne et al (1973), Onuchin & Telnov (1974), and other work cited by them. In Figure 9 we show the distributions obtained by Harris et al (1973) for the energy loss in 1.5 cm of argon/7% CH_4 at normal density. Data on the relativistic rise in argon and xenon are shown in Figures 10 and 11. Reliable data for propane are also available. The

¹⁰For convenience we use this term for the experimental as well as the theoretical distributions, remembering that the former is really the ionization distribution as discussed in Section 3.2.

pressure dependence of the rise has been studied extensively by Walenta et al (1979), Fancher et al (1979), and Hasebe et al (1978).

The dashed lines on Figures 9–11 are the predictions of the most general model, due to Sternheimer (1952) based on the work of Landau (1944). The basic assumption of Landau's model is that the Rutherford term in the cross section is the only significant source of statistical fluctuation responsible for the distribution width and that the contribution of the cross section in the resonance region may be evaluated in the low density limit by using the oscillator strength sum rule to give a "restricted mean energy loss." This depends only on the mean ionization potential defined by $\ln I = \int \ln(\hbar\omega) f(\omega) d\omega$, and not on details of the optical oscillator strength, $f(\omega)$. The density effect is described by a correction term (Sternheimer 1952, Sternheimer & Peierls 1971 and other references cited there). The model provides a poor description of the distributions (Figure 9) and the relativistic rise (Figures 10, 11). In particular the calculated rise is some 10–

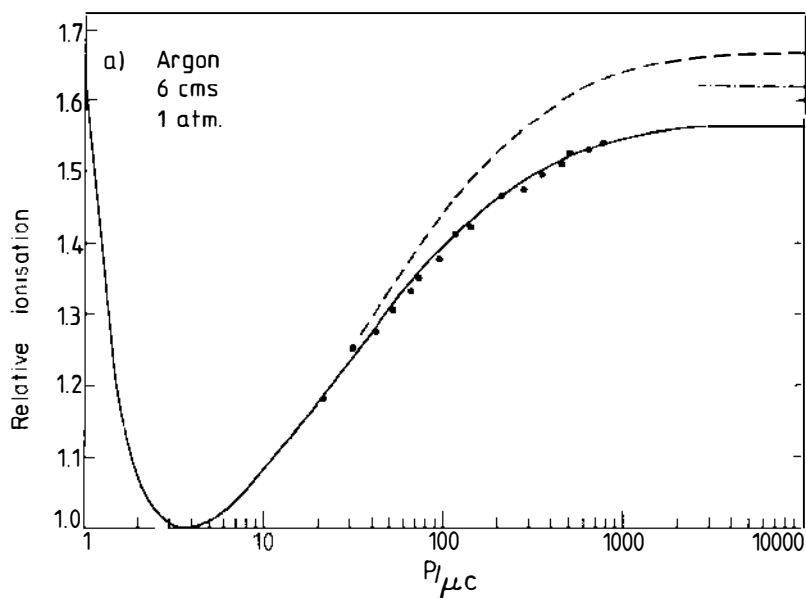


Figure 10 Values of ionization in argon at normal density (relative to $\beta\gamma \sim 4$). Measured points from Lehrs et al (1978) refer to the mean of the lowest 40% of 128×6 -cm samples of argon/5% CH_4 and, with the exception of the highest point, were taken with incident hadrons. The experimental errors are slightly larger than the points shown. The dash line and dash-dot line are the predictions of the Sternheimer (1952) and Ermilova et al (1977) models respectively. The solid line is the most probable energy loss in 4.5 cm of pure argon calculated with the PAI model.

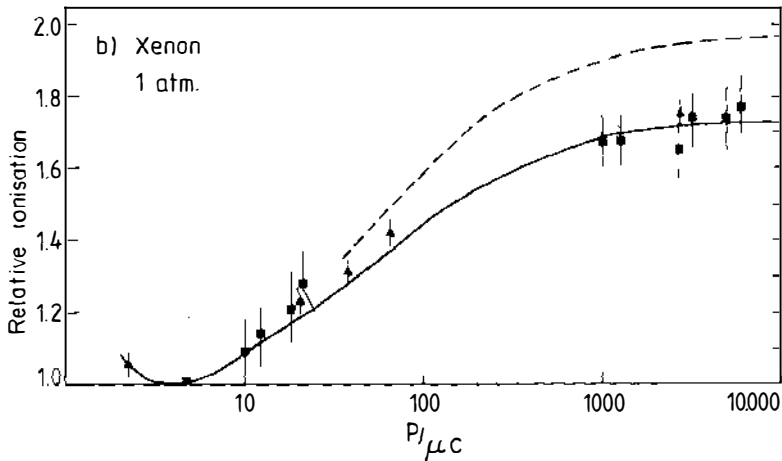


Figure 11 Relative ionization in xenon at normal density taken from Fischer et al (1975) (triangles), Walenta et al (1979) (squares), "most probable" values for 1.27 cm of xenon/18% methylal, and 2.3 cm of xenon/7.5% CH₄/5% C₃H₈ respectively. The data above $\beta\gamma = 1000$ were taken with incident electrons; the remainder with hadrons. Dashed line is the prediction of the Sternheimer (1952) model and solid line is that of Cobb et al (1976) for pure xenon.

15% too large for the noble gases¹¹. Recently Chechin & Ermilova (1976) discussed the range of validity of the Landau model. Landau's basic assumption is expected to fail for thicknesses x such that $\xi/I < 100$ where $\xi = 2\pi Ne^4 x / m\beta^2 c^2$. For relativistic particles in argon, xenon, and propane this corresponds to a minimum thickness of about 170, 150, and 30 cm atm respectively. On the other hand, for efficient particle identification, ionization must be measured in a number of samples, each thin enough to distinguish the spread due to the large fluctuations of the Rutherford contribution from the resolution due to fluctuations in the resonance region. This requires $\xi/I \sim 1$, incompatible with the basic assumption of the Landau model. An early attempt to improve the description of the distributions included a first-order atomic shell effect (Blunck & Leisegang 1950), but the model is not applicable for $\xi/I < 10$ (Chechin & Ermilova 1976).

More recent models have developed along the lines discussed in Section 2. Simple models of this type, by including the shell structure of the atoms describe the energy-loss distribution with fair success; the detailed

¹¹ A conjecture by Garibyan & Ispiryan (1972) that this is a transition effect due to the chamber windows has not been confirmed by the experiments of Smith & Mathieson (1975) or Allison et al (1976).

treatment of the dielectric constant is necessary to achieve a good description of the relativistic rise. For example, Ispiryan et al (1974) and Talman (1979) used as a crude model of the photoabsorption spectrum a number of δ functions representing the fraction f_i of electrons in each shell at an energy $E_i = 1.3 \times$ the energy of the shell edge. The cross section in Equation 28 then becomes in the low density limit

$$\frac{d\sigma}{dE} = -\frac{2\pi e^4}{mc^2\beta^2} \frac{f_i}{E_i} \delta(E-E_i) \left(\ln \frac{2mc^2\beta^2\gamma^2}{E_i} - \beta^2 \right) + \frac{2\pi e^4}{mc^2\beta^2} \frac{f_i}{E^2} H(E-E_i), \quad 42.$$

where H is a unit step function.

The continuous curves superimposed on Figure 9 are the result of a calculation using the PAI model for pure argon. Use of Equation 42 produces similar results at least for 3-GeV/c pions. Taking into account the quoted energy normalization uncertainty of 20% in the data, the agreement is fair although there is an excess of signals at small energy loss also noted in other data (Allison et al 1979). The experimental resolution function (Equation 41) has not been included in the calculation but has a small effect.

Ermilova et al (1977) calculated the energy loss on the Fermi plateau using the empirical photoabsorption spectrum, although this was done earlier in connection with the track density in bubble chambers by Chechin et al (1972). Substituting the approximate Formula 32 for the first two terms of Equation 28 yields

$$\frac{d\sigma}{dE} = \frac{\alpha}{\beta^2\pi} \frac{\sigma_\gamma(E)}{EZ} \left[\ln \left(\frac{\omega 2mc^2\beta^2}{\omega_p^2 \hbar} \right) - 1 \right] + \frac{\alpha}{\beta^2\pi} \frac{1}{E^2} \int_0^E \frac{\sigma_\gamma(E')}{Z} dE' \quad 43.$$

for the cross section. In their treatment Ermilova et al (1977) took the logarithmic term to be the only contribution to the restricted energy loss. With these approximations they overestimated the relativistic rise of argon as shown on Figures 10 and 11. Cobb (Cobb 1975, Cobb et al 1976, Bunch 1976) was the first to use the full cross section (Equation 28), although he and his colleagues approximated the photoabsorption cross section by a series of Lorentzians or δ functions similar to the model of Ispiryan et al (1974). The energies chosen were equal to the values of the absorption edges. This choice was criticized by Ermilova et al (1977). However, the calculations gave very good agreement with available data on the relativistic rise for both argon and xenon (Figure 11). (Increasing the ionization energies by 30% as suggested by Ermilova et al increased the calculated relativistic rise by about 3% for argon.) Figure 10 shows the results of new calculations with the PAI model for pure argon. They are in agreement with the data of Lehraus et al (1978).

We conclude that (a) for thin absorbers the Landau-Sternheimer model is

inapplicable; and (b) the PAI model provides a good description of the data although further examples, including the effects of quenching gases, remain to be calculated. Possible residual differences between calculation and experimental data, for instance in the width of the spectra, may be due to a breakdown of the assumed correspondence between energy loss and measured ionization.

4 MULTIPLE SAMPLING DETECTORS

4.1 Statistical Analysis of Signals

Let us consider how the ionization resolution and thence velocity and mass resolution may be obtained in practice. This problem was first considered by Alikhanov et al (1956). As discussed in the introduction a detector capable of distinguishing between different mass assignments to a track of known momentum must make a large number n of measurements Δ_i . The most probable energy loss is a very poor estimator for a spectrum with limited statistics. In principle the most efficient use of the data to distinguish between two mass hypotheses is to compute the likelihood ratio

$$L_{12} = \prod_{i=1}^n F_1(\Delta_i)/F_2(\Delta_i) \quad 44.$$

where F_1 and F_2 are the normalized pulse height distributions expected for two masses μ_1 and μ_2 and L_{12} is the likelihood ratio of μ_1 to μ_2 . The distributions F vary little in shape with velocity¹². For example Figure 12 shows the calculated dependence of the relative width on the most probable energy loss for argon according to the PAI model. The small variation with $\beta\gamma$ is due to the dependence on the statistics of both the total number and the relative numbers of hard and soft collisions.

For practical detectors we may assume that the shape of F is velocity invariant¹³ and find the most likely values and error of the ionization scale

¹² To the extent that this is true the dependence of different ionization estimators on velocity is the same for a given sample thickness. This is assumed in Figures 10 and 11 where ratios of "most probable" values and truncated mean values are compared indiscriminately.

¹³ The loss of information associated with this simplification is not serious. It has been suggested (Nygren 1976, Talman 1979) that kaons and pions might be separated by the different widths of their distributions in the region of minimum ionization. Careful study shows that this is a false hope (Allison et al 1978a). A likelihood ratio analysis using the PAI model shows that more than 5000×1.6 -cm atm samplings in argon would be required to separate K and π by two standard deviations. Talman (private communication) has agreed that this identification is impracticable. His original paper erroneously assumes that the log likelihood function is parabolic in the neighborhood of the double solution.

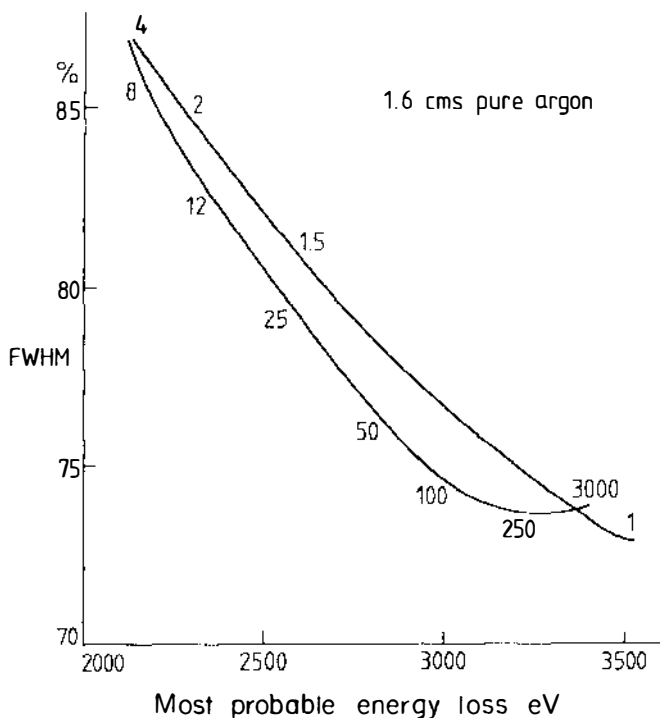


Figure 12 Relative width of the energy-loss distribution as a function of the most probable energy loss for 1.6 cm of pure argon at normal density calculated with the PAI model. The figures on the graph are the corresponding values of $\beta\gamma$.

parameter λ which maximizes

$$L(\lambda) = \prod_{i=1}^n F(\Delta_i/\lambda) \quad 45.$$

for each track. Our simulation studies show that $\ln \lambda$ is normally distributed and that the relative values of λ obtained for different tracks are insensitive to the precise form of the function used. By monitoring the average value of λ fitted to, for instance, beam tracks of known velocity, a normalized ionization estimate and error for each track can be determined¹⁴. The probability of a certain mass assignment to a track may then be calculated by comparing the expected ionization (based on the known momentum, the

¹⁴ In a practical detector the sample length depends on track inclination. If it is assumed that the shape F is unaffected, the likelihood method may be used as described and the fitted value of λ corrected by a simple $\cos \theta$ factor. This approximation is probably satisfactory for inclinations up to about 45° .

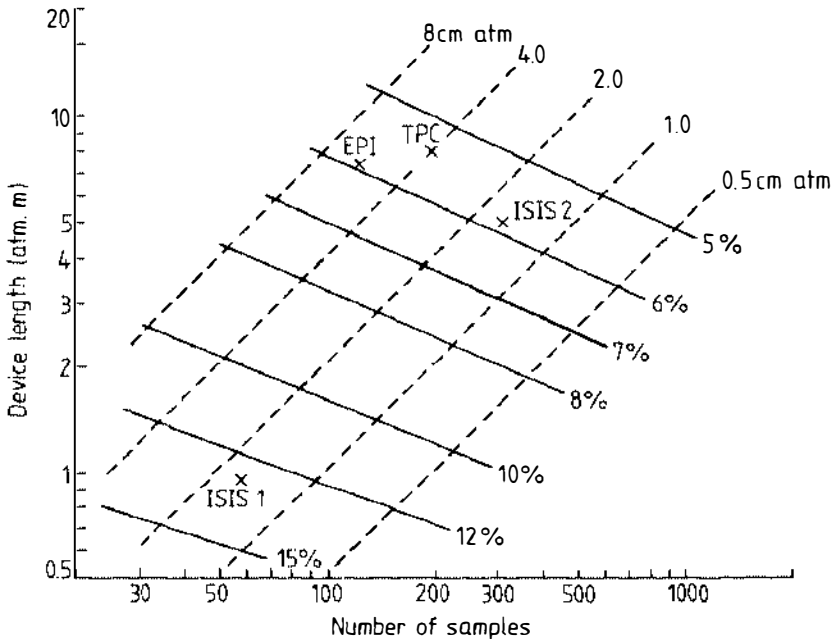


Figure 13 The ionization resolution (% FWHM) of a multisampling detector filled with pure argon calculated with the PAI model for $\beta\gamma = 100$. The dashed lines are loci of constant sample thickness. The devices EPI, ISIS1, ISIS2, and TPC are described in Table 2.

relativistic rise curve, and the hypothesized mass) with the observed ionization value and error using normal error statistics.

Although the likelihood method is efficient, some authors have considered it too time consuming in practice and have studied other methods. If the energy-loss distribution were Gaussian, it would be sufficient simply to take the mean of all measurements. Unfortunately this is not possible because of the long tail. However, this difficulty may be overcome by taking a fixed fraction r of the signals with the smallest amplitudes and evaluating their mean. This procedure has been studied by Alikhanov et al (1956) and many workers in the field since. They find the resolution insensitive to the value of r chosen in the range 0.4–0.6, and little worse than that obtained by the likelihood method. However, we believe that the likelihood method should not be ignored; there is a negligible loss of information if the data are histogrammed in coarse bins¹⁵ and, if the median of the distribution is used

¹⁵ This implies that the “least count” in the measurement of the ionization may also be coarse; 4–5 bits of precision are more than sufficient. However, the stability must be much better than this and 8 bits or more are usually used.

to derive a good starting value, a maximum likelihood fit can be carried out rapidly.

Figure 13 is a plot of the calculated ionization resolution obtainable from a likelihood analysis of data from devices using pure argon at $\beta\gamma = 100$. Lines of constant resolution (FWHM) are shown as a function of the device length and number of samples. Crosses show the length and number of samples for four devices currently operational or under construction. The gas in these devices is not pure argon but this has a small effect. The external particle identifier (EPI) has achieved 6% (FWHM) ionization resolution (Lehraus et al 1978) and ISIS1 between 12 and 14% (Allison et al 1979). Both of these figures are in good agreement with the predictions shown on Figure 13.

4.2 The Choice of Detector Parameters

The parameters that determine the mass resolution of an ionization detector are the number of samples n , the sample size x , the gas composition, and the gas pressure P . These influence the ionization resolution, the slope of the relativistic rise, and the $\beta\gamma$ value at which the density effect becomes important.

A study of a wide variety of gases and conditions has not yet been carried out using the PAI model. Instead, in Table 1 we show the results of calculations with an earlier model by Cobb et al (1976) for some gases at normal density. These show that, while the ionization resolution for the rare gases is comparable, the resolution for low- Z molecular gases is better.

Table 1 Calculations of resolution in 5 m of gas at normal density divided into 1.5-cm samples (from Cobb et al 1976)

Gas	Relativistic rise	Ionization resolution (% FWHM)	K/ π ^a limit (GeV/c)
Helium	1.41	5.2	45
Neon	1.54	5.4	50
Argon	1.58	5.3	55
Krypton	1.60	5.2	55
Xenon	1.70	5.5	95
Methane	1.36	3.9	30
Ammonia	1.39	4.2	45
Nitrogen	1.48	4.6	45
Carbon dioxide	1.45	3.9	50
Argon/20% CO ₂	1.55	4.9	55

^a The K/ π limit corresponds to the momentum at which K and π mesons are separated by $1.8 \times$ FWHM resolution.

However, this apparent advantage is more than offset by the smaller relativistic rise. Among the rare gases the rise is largest for high Z . The behavior of both the resolution and the relativistic rise is a direct consequence of the size of energy transfer in a typical collision, as discussed in Section 2.5. The experimental data of Walenta et al (1979), who compare propane, argon, and xenon, confirm these trends. Therefore to get the best mass resolution over the widest range of $\beta\gamma$, heavy noble gases are preferred. Xenon has not yet been used; energy-loss detectors are usually filled with argon and a small component of a molecular gas to ensure their operation as drift or proportional chambers.

We now consider more generally whether there are any simple optimum choices of detector parameters and gas composition. To do this we derive some approximate formulae based on the PAI model and supported by experimental data. They are intended as a guide only; they are not a substitute for a calculation using the photoabsorption data for the gas mixture concerned.

For pure argon the ionization resolution $R(\% \text{ FWHM})$, shown in Figure 13, is adequately described by the formula

$$R = 96n^{-0.46}(xP)^{-0.32}. \quad 46.$$

One expects the power of n to be -0.5 ; Walenta et al (1979) found a power -0.43 empirically using a truncated mean analysis rather than a maximum likelihood method. Figure 14 shows experimental data for the relative widths of single sample distributions ($n = 1$) as a function of the dimensionless scaled value of x , namely $\xi/I = 2\pi Ne^4 x / m\beta^2 c^2 I$. Numerically ξ

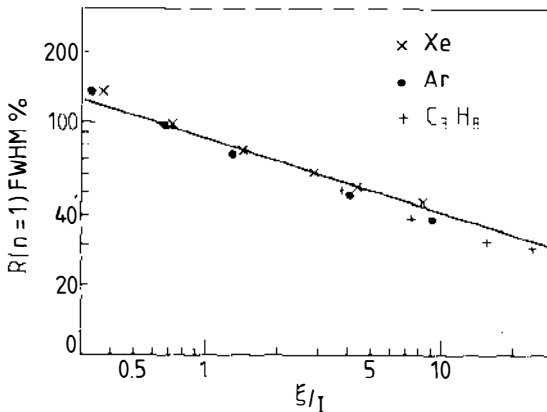


Figure 14 Experimental data on the width of the energy-loss distribution (Walenta et al 1979) as a function of the scaled sample thickness ξ/I . The solid line is the extrapolation of Equation 46 for pure argon to a single sample ($n = 1$).

$= 6.83\nu xP/\beta^2$ where ν is the mean number of electrons per molecule and xP is in cm atm. I is the mean ionization potential defined in Section 3.3. Equation 46 gives a fair description of the data, not only for argon, but for xenon and propane as well in the case $n = 1$. Extending the formula to $n \neq 1$ for all gases by working in terms of ξ/I in place of xP , we find

$$R = 81n^{-0.46}(\xi/I)^{-0.32}. \quad 47.$$

Judging from Figure 14, this formula is good to 10–20% in the range $0.5 < \xi/I < 10$.

The slope of the log rise below the onset of the density effect depends on the gas mixture and on the sample thickness. This may be seen by examining Equation 26 in the low density limit ($\epsilon_1 = 1$),

$$\begin{aligned} \langle dE/dx \rangle = & - \int_0^\infty d\omega \frac{e^2}{\beta^2 c^2 \pi} \left[\frac{Nc\sigma_\gamma(\omega)}{Z} \left(\ln \frac{2m\beta^2\gamma^2 c^2}{\hbar\omega} - \beta^2 \right) \right. \\ & \left. + \frac{1}{\omega} \int_0^\infty \frac{\sigma_\gamma(\omega')}{Z} d\omega' \right]. \end{aligned} \quad 48.$$

The dependence of the slope on gas composition is through the $\hbar\omega$ denominator in the logarithm, which results in a form

$$S = \frac{200 \ln 10}{\ln(2m\beta^2\gamma^2 c^2) - 1 - \ln I + \chi} = \frac{460}{15.6 - \ln I + \chi} \quad 49.$$

where S is the slope in percent per decade (of $\beta\gamma$) relative to minimum ionization ($\beta\gamma = 4$); χ describes the contribution of the last term in Equation 48, the Rutherford or quasi-free term, which exhibits no log rise. Its magnitude is about 0.5 for ξ/I near 1 and increases slowly with sample thickness as further contributions from quasi-free scattering get folded into the main peak of the energy-loss distribution. This reduces the slope of the relativistic rise for thicker samples. The effect is very clear in the data of Walenta et al (1979) for propane, argon, and xenon. These data may be described empirically by the expression

$$S = (\xi/I)^{-0.2} \frac{430}{16 - \ln I}, \quad 50.$$

which is close to the expected form (Equation 49). The first factor describes the dependence on sample width over the range covered in Figure 14 and shows that the slope increases by 15% if the sample thickness is halved. The second factor gives the dependence on gas mixture; for example, the slope is 10% greater in xenon than argon. For molecular gases ξ/I is larger and, in general, $\ln I$ is smaller than for rare gases so that the slopes are lower on both counts.

The density effect starts to modify the slope as soon as the velocity dependence of collisions with the outer shells of electrons saturate. As shown in Section 2.5 this happens over the $\beta\gamma$ range ε/E_p to $2\varepsilon/E_p$, where ε is related to the outer shell binding energy and E_p is the plasma energy ($E_p = 0.19 (\nu P)^{1/2}$ eV). At higher $\beta\gamma$ the slope falls progressively. No simple formula is available and the detailed behavior must be calculated for the conditions concerned. Nevertheless the choice of low pressure (small E_p) noble gases (large ε) is favored.

For velocities below the onset of the density effect we may calculate the mass resolution for particles of known momentum using Equations 47 and 50:

$$\begin{aligned}\delta(\ln \mu) &= \delta(\ln \beta\gamma) = \frac{\lambda}{\lambda_0} R \ln 10/S \\ &= 0.43 \frac{\lambda}{\lambda_0} n^{-0.34} (n\xi/I)^{-0.12} (16 - \ln I),\end{aligned}\tag{51}$$

where λ/λ_0 is the ionization relative to minimum. This formula shows that in this region the mass resolution is very insensitive to the gas mixture (I), rather insensitive to the total mass of gas ($n\xi$), and only depends significantly on n . We conclude that the only real way to improve the mass resolution of an energy-loss detector below the onset of the density effect is to sample the ionization as finely as possible.

For very thin samples where ξ/I is much less than one, the shape of the energy-loss distribution will show structures due to the energy spectrum of single collisions. It follows that the shape of the distribution will not scale as assumed in Section 4.1 and the analysis discussed above will not be applicable. The velocity and mass resolution of such fine grain ionization data is ultimately limited by the statistics of the energy-loss collisions rather than by imperfect sampling. Such an ideal detector was discussed at the end of Section 2.5. There are practical problems in the measurement of fine grain energy-loss data in drift chambers. These have been studied experimentally by Rehak & Walenta (1980) and in simulation by Lapique & Puiz (1980). The main problems are the loss of resolution due to electron diffusion in the gas and the large fluctuations of the gas amplification for single electrons. Primary ionization has also been studied in other ways; by counting streamers in low density gases in a streamer chamber (Davidenko et al 1969, Eckardt et al 1977), by measuring the efficiency of spark chambers (Söchting 1979), and by observing the time-jitter of proportional chamber signals (Rehak & Walenta 1980). The streamer chamber method has been developed for individual particle identification, and Eckardt et al (1977) achieved an ionization resolution of 19% (FWHM) on a 90-cm track

length in a helium-neon mixture. The method is currently limited by the difficulty of resolving clusters from different collisions.

4.3 *Practical Considerations*

So far we have discussed only the principles of energy-loss detectors without considering how they may be put into practice. In this section we mention briefly some of the practical considerations, discussed in greater detail in the references cited.

In general an energy-loss detector will be large, 15 m^3 or more, its length being determined by the path length necessary to achieve a given mass resolution and its aperture by the geometrical acceptance. The practical problem is to instrument this large volume. In experiments at storage rings, at least, the detector will be inside the magnetic field volume and perform the dual function of particle identification and momentum analysis. The many samplings of the particle "track" will provide a high degree of information redundancy for pattern recognition. Although there is no fundamental conflict between obtaining coordinate and energy-loss information, an energy-loss detector is seldom optimized for its performance as a particle identifier alone. The practical solution is a detector employing drift chamber techniques but using electron drift paths that are long compared with conventional drift chambers, the length being related to the expected particle flux through the detector.

In such a detector each track is sampled by drifting the ionization electrons to a uniformly spaced array of anode wires under the influence of a high uniformity electric field. Proportional gas amplification then takes place at each wire, and the ionization sample is identified with the charge, which is the integral of the current signal from the wire. The shape of this signal varies with the angle of the track and the drift distance through the effect of electron diffusion. As a result, to avoid bias, it is necessary to measure a shape-independent integral (Pleming 1977). The shorter the sample size, the smaller the component of pulse width due to track inclination and the better the multitrack resolution of the detector. The ability to handle high multiplicities and high rates means that considerable attention must be paid to the elimination of baseline shifts in the electronics (Brooks et al 1978).

For each track the pulse heights of many signals must be collected with systematic errors of less than 1%. The extent of cross talk or correlation between these signals, which are treated as independent, is of outstanding importance. The average cross talk between *any* two signals needs to be less than about 3×10^{-4} ; this affects the design of the electronics, power supplies, and grounding. The correlation between signals from neighboring samples in the detector can be larger ($\sim 10^{-1}$) without affecting the

resolution. Delta-ray electrons passing from one sample to another are too few to cause problems in detectors with good spatial resolution; such low energy electrons are quickly separated from the parent track by multiple scattering. In the presence of a magnetic field they are trapped in the original sample. Capacitive coupling between wires may be reduced by the use of intermediate field wires between collecting anodes (Allison et al 1976). Cross coupling due to electron diffusion is important for long drift-path detectors but can be minimized by a careful choice of gas mixture (Allison et al 1974). Although the effect of *linear* cross talk on the average pulse height is zero, it does change the shape of the asymmetric ionization distribution slightly. Practical reasons against a choice of very small sample width include the electromechanical stability of large arrays of close wires, the mechanical tolerances needed for uniform gas amplification, the small signal amplitudes, and the cost of the electronics.

In order that individual track signals may be sensed and integrated without bias there must be an adequate signal-to-noise ratio. This depends on the bandwidth of the electronics, the electronic noise, the number of ionization electrons, and the gas amplification factor (Pleming 1977). The gas amplification cannot be increased beyond about 10^4 without the risk of angle-dependent saturation effects (Frehse et al 1978, Allison et al 1978c). More significantly, for long drift-path geometries the production of positive ions in the gas amplification produces a volume space charge that distorts the drift field (Allison et al 1974, 1979, Friedrich et al 1979). To avoid this effect, the flux, gain, drift distance, or duty cycle of the device must be limited. Considerable attention must be paid to gas purity, especially with the longer drift paths, if the ionization electrons are not to be lost by attachment to electronegative molecules. Typically the concentration of oxygen, as the dominant electronegative impurity, must be kept in the range 0.1–1.0 parts per million (Allison et al 1974, 1979).

In Section 4.2 it was shown that, at velocities for which the density effect is unimportant, the mass resolution is more or less independent of the choice of gas (at constant mass of gas). In practice consideration of systematic effects modifies this conclusion. For gases with higher I the variation of ionization with velocity is larger and the ionization resolution worse than for those with lower I (Equations 47 and 50). Gases with higher I are therefore to be preferred since the mass resolution is less sensitive to systematic and calibration errors. Sources of these are associated with the density sensitivity of the gas amplification factor and mechanical tolerances of the chamber. Some care is required to reduce these errors to the level of 1%.

Data from a single event with 10 or more tracks and several hundred signals per track amount to typically 10^5 bits of information. These data

Table 2 Relativistic energy-loss particle identifiers (May 1980)

Name	Gas	Samples (cm)	Acceptance	Physics objective ^a	Status
EPI ^a	Ar/5% CH ₄ 1 atm	128 × 6	2m × 1m	diffraction dissociation with BEBC (CERN)	Data 1978
ISIS1 ^b	Ar/20% CO ₂ 1 atm	80 × 1.6	4m × 2m	Strong interaction and charm physics with EHS (CERN)	{ Data early 1980 Construction
ISIS2 ^b	Ar/20% CO ₂ 1 atm	320 × 1.6	4m × 2m		
CRISIS ^c	Ar/20% CO ₂ 1 atm	192 × 1.6	1m × 1m	Hadron physics with FHS (FNAL)	Construction
JADE ^d	Ar/C ₂ H ₆ 4 atm	48 × 1	~4π	e ⁺ e ⁻ at PETRA	Data 1979
TPC ^e	Ar/20% CH ₄ 10 atm	192 × 0.4	~4π	e ⁺ e ⁻ at PEP	Construction
UA1 ^f	Ar/C ₂ H ₆ 1 atm	200 × 0.8	~4π	p̄p collider at CERN	Construction

^a Jeanne et al 1973, Lehraus et al 1978, and Figure 13.

^b Allison et al 1974, 1978b, 1978c, 1979, and Figure 13.

^c Wadsworth et al 1979.

^d Barber et al 1976, Farr et al 1978, Wagner et al 1980.

^e Nygren 1976, Fancher et al 1979, and Figure 13.

^f Astbury et al 1978.

^{*} BEBC = Big European Bubble Chamber; EHS = European Hybrid Spectrometer; FHS = Fermilab Hybrid Spectrometer.

collected by drift chambers in a few microseconds represent a peak rate to the electronics of about 10^{10} Hz. The design of the electronics must aim at performing a parallel-to-serial conversion so that the data reach a computer at a manageable rate. Indeed the use of long drift paths in the chambers is the first stage of such a parallel-to-serial conversion. Analogue storage techniques on discrete capacitors (Brooks et al 1978, Farr & Heintze 1978) or on charge-coupled devices (Fancher et al 1979) have been used; other possibilities such as “flash” analogue-to-digital converters were reviewed by Dhawan & Ludlum (1978).

4.4 Existing Detectors

Following the initial idea of a relativistic particle identifier based on energy loss (Alikhanov et al 1956), and the exploratory work of Ramana Murthy & Demeester (1967) and Dimcovski et al (1971), Jeanne et al (1973) proposed a full-scale device known as the external particle identifier (EPI) to operate behind the BEBC bubble chamber at CERN. The device consists of 4096 independent rectangular proportional counters defined by planes of cathode wires. Its acceptance is modest and its multitrack capability is limited by the small number of transverse cells. Its mass resolution, however, is excellent as shown in Figure 3. Table 2 gives a list of devices now operating or under construction. Most of these have been reviewed by Heintze (1978). Apart from EPI they all make extensive use of long electron

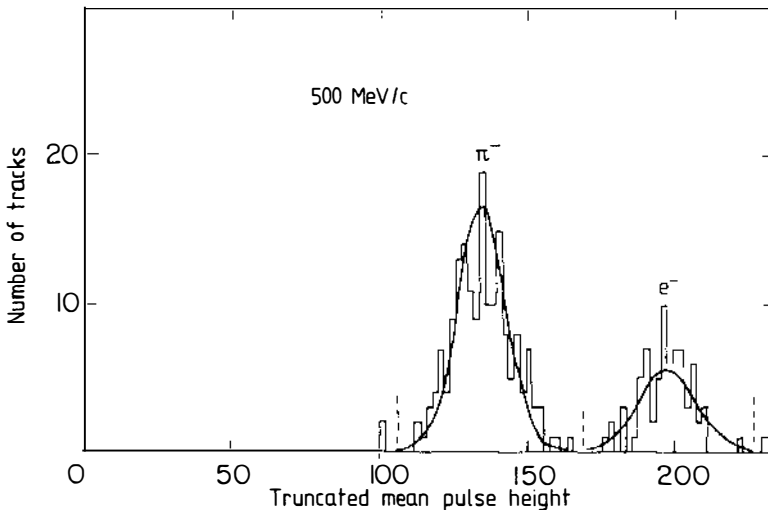


Figure 15 Results of the ISIS1 test showing separation between individual electrons and pions at 500 MeV/c. The truncated mean is the mean of the lowest 36 of the 60 samples. The curves represent ionization resolutions of 12 and 14% (FWHM) respectively.

drift paths. JADE, the TPC, and the UA1 detectors are designed for colliding-beam machines and have cylindrical geometries within the magnetic field volume where it is difficult to achieve the necessary track length and the design must be optimized for momentum as well as mass resolution. The relativistic particle identification capabilities of JADE and UA1 are marginal. By working with argon at 10 atm, the TPC is expected to have good mass resolution up to 15 GeV/c.

The situation is easier for fixed-target experiments where space allows the use of normal pressure gases and dedicated particle identifiers. The ISIS2 chamber is expected to achieve good mass resolution in a fiducial volume of 40 m³ with only 320 channels of electronics by using drift paths of up to 2 m. A similar but much smaller device, CRISIS, is under construction for use at FNAL (Wadsworth et al 1979). Tests with ISIS1 have shown the expected mass resolution (Figure 15; Allison et al 1979). Figure 16 shows a plot of the position information for drifted tracks recorded by ISIS1. The high density of spatial information, the clear identification of background signals (δ rays

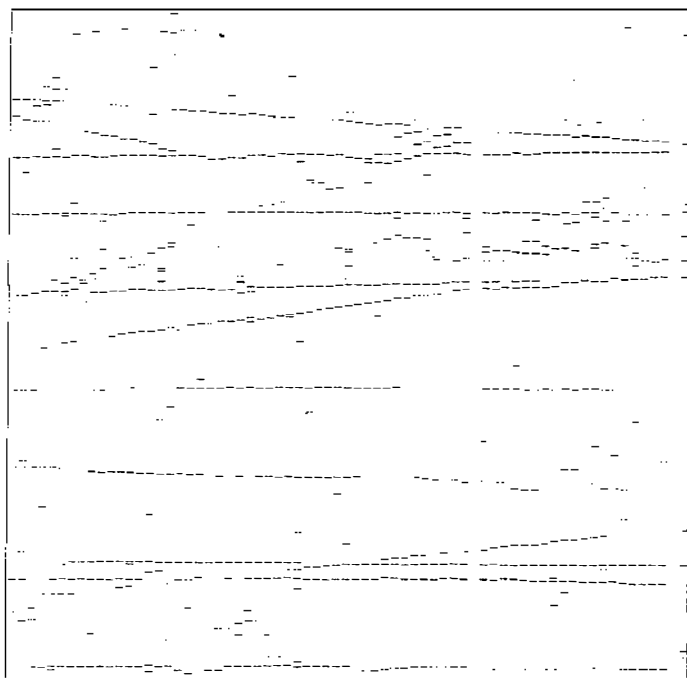


Figure 16 A typical plot of coordinate data showing a fair number of tracks passing through ISIS1 during a test. The ordinate is the drift time and the abscissa is the sample or wire number. Pulse height information is also recorded for each "hit" shown.

etc), and the good multitrack resolution are apparent. As a result, clear sections of each track, free of contamination by other signals, can be distinguished and unbiased ionization estimates obtained for a high multiplicity of tracks.

5 SUMMARY

Spectacular progress has been made since Alikhanov et al (1956) first described in detail the formidable practical problem of identifying relativistic charged particles by energy loss. Recent tests with large detectors indicate that these problems have been overcome and that we may now look forward to the successful application of the method to provide particle identification in high energy physics experiments.

With the advances in practical application have come a better theoretical understanding and more thorough calculations. These are now able to give a good description of data for energy loss in thin samples ($\xi/I \sim 1$, equivalent to about 1 cm atm of argon). More clean data would be welcome for a variety of gases at different densities and thicknesses and for a range of $\beta\gamma$ values. Nevertheless it is now possible to predict the mass resolution of a detector with confidence. Calculations point to argon or, better, xenon as the best gas, with the choice of density governed by a compromise between the constraint of detector length and mass resolution at high $\beta\gamma$. The only way to improve the resolution within this constraint is to sample more finely.

Further efforts continue to develop much finer grain ionization detectors although these present significant practical difficulties. We note that the mass resolution of the "ideal" detector, which resolves the energy loss in individual atomic collisions, is a factor 2.5 or so better than current detectors at lower values of $\beta\gamma$ (less than 50 for argon). At higher values of $\beta\gamma$ where an improved resolution would be most welcome, the factor is significantly smaller.

ACKNOWLEDGMENTS

We would like to thank Drs. L. Lyons, M. Inokuti, and W. G. Scott for their valuable comments and careful reading of drafts of the manuscript. Finally we thank Miss Daphne Pollard for her patience and skill in typing the manuscript.

APPENDIX

A picture of the field of a relativistic charged particle in a medium

The main features of the logarithmic rise of the energy-loss cross section, the density effect, and their relationship with Cerenkov radiation depend only on the virtual wave structure of the electromagnetic field of the incident particle and may be understood with the aid of a simple model.

Consider a scalar field ϕ coupled to a particle moving with constant velocity v along the x axis through a dispersive medium in which the phase velocity of the field is $u(\omega)$, a function of frequency. In the rest frame of the particle the field is static. In the frame of the medium it is a wave packet that is neither dispersed nor attenuated and that moves along x with constant amplitude and phase with respect to the particle. Thus the phase velocity along x of each frequency component must equal v since it is a component of a static field as seen by an observer moving with the particle, $v = \omega/k_x$ (k is the wave number of the Fourier component of frequency ω). By definition of the phase velocity, $u = \omega/|k|$. Therefore the space-time dependence of each frequency component is described in the 2-dimensional case¹⁶ by the phase factor $\exp i(k_x x + k_y y - \omega t) = \exp i \omega/v [x - vt + (v^2/u^2 - 1)^{1/2} y]$. The dimensionless velocity $v/u(\omega)$ may be denoted by $\beta'(\omega)$. If β' is less than unity, the transverse dependence of the field will be an evanescent wave of range $y_0(\omega) = v/\omega(1 - \beta'^2)^{-1/2} = \beta'\gamma'\lambda$ where $\gamma'(\omega) = (1 - \beta'^2)^{-1/2}$ and λ is the free wavelength over 2π . For larger velocities β' gets closer to unity and the range increases linearly with $\beta'\gamma'$. If v becomes greater than u , the field is a traveling wave and there is a flux away from the source at an angle $\arccos(1/\beta')$. These features of wave motion are common to, for example, acoustic and surface waves.

For the electromagnetic field of a charged particle moving in vacuum, $u = c$ for all frequencies $\beta' = v/c$ and $\gamma' = \gamma$. The expansion of the electromagnetic field with $\beta\gamma$ responsible for the relativistic rise is therefore seen as a general consequence of wave motion. In a medium, on the other hand, $u = c/(\epsilon)^{1/2}$ where $\epsilon(\omega)$ is the dielectric constant. There are two cases:

(a) $\epsilon(\omega) > 1$. Below the velocity $\beta = 1/(\epsilon)^{1/2}$ the transverse waves are evanescent. Above this velocity free radiation is emitted insofar as the medium is transparent. This is Cerenkov radiation and occurs mainly in the region of ω below ionization threshold.

(b) $\epsilon(\omega) < 1$. In this case, the range is now $y_0(\omega) = v/\omega(1 - \beta^2\epsilon)^{-1/2}$, which has a limiting value of $\lambda(1 - \epsilon)^{-1/2}$. Ninety percent of this range is achieved by a $\beta\gamma$ value of $2(1 - \epsilon)^{-1/2}$ where the field saturates, becoming insensitive to

¹⁶ In the 3-dimensional problem the exponent in y is replaced by a Bessel function in the cylindrical polar coordinate r . However, the qualitative features are unaltered.

any further increase of velocity. Using a crude model of the dielectric constant, $\epsilon(\omega) = 1 - \omega_p^2/\omega^2$, we see that the energy-loss cross section is expected to saturate at $\beta\gamma = 2\omega/\omega_p$. This expectation is confirmed by proper calculation and comparison with experiment in this paper.

Alternatively the quanta of the electromagnetic field in the medium may be considered as having an "effective mass," similar to the concept of effective mass ascribed to electrons in the band theory of solids. Normal modes of the field satisfy the equation $c^2k^2 - \omega^2\epsilon(\omega) = 0$ whence $m(\omega) = \hbar\omega/c^2 [1 - \epsilon(\omega)]^{1/2}$. The exchange of such photons represents a short range force limited by their Compton wavelength, which is equal to $\lambda(1 - \epsilon)^{-1/2}$, the same result as obtained above.

Literature Cited

- Alikhanov, A. I. et al. 1956. *Proc. CERN Symp. on High Energy Accelerators Pion Phys.* 2: 87-98
- Allison, W. W. M. et al. 1974. *Nucl. Instrum. Methods* 119: 499-507
- Allison, W. W. M. et al. 1976. *Nucl. Instrum. Methods* 133: 325-34
- Allison, W. W. M. 1977. Presented at *Int. Symp. on Transition Radiat. High Energy Part. Yerevan, USSR*. Oxford, OUNPL33/77
- Allison, W. W. M., Bunch, J. N., Cobb, J. H. 1978a. *Nucl. Instrum. Methods* 153: 65-67
- Allison, W. W. M. et al. 1978b. *Nucl. Instrum. Methods* 156: 169-70
- Allison, W. W. M. et al. 1978c. The design of ISIS and the results of tests with ISIS1. *CERN/EP/EHS/PH78-10*
- Allison, W. W. M. et al. 1979. *Nucl. Instrum. Methods* 163: 331-41
- Astbury, A. et al. 1978. A 4π solid angle detector for the SPS used as a proton-antiproton collider at a centre of mass energy of 540 GeV. *Proposal CERN/SPSC/P92*
- Barber, D. P. et al. 1976. A proposal for a compact magnetic detector at PETRA. Hamburg: DESY
- Berg, R. A., Green, A. E. S. 1973. *Adv. Quantum Chem.* 7: 277-88
- Bethe, H. A. 1930. *Ann. Phys.* 5: 325-400
- Bethe, H. A., Jackiw, R. W. 1968. *Intermediate Quantum Mechanics*, pp. 302-5. New York: Benjamin. 2nd ed.
- Bichsel, H., Saxon, R. P. 1975. *Phys. Rev. A* 11: 1286-96
- Blunck, O., Leisegang, S. 1950. *Z. Phys.* 128: 500-5
- Bohr, N. 1913. *Philos. Mag.* 25: 10-31
- Bonham, R. A. et al. 1978. *Adv. Quantum Chem.* 11: 1-32
- Brooks, C. B. et al. 1978. *Nucl. Instrum. Methods* 156: 297-99
- Budini, P., Taffara, L. 1956. *Nuovo Cimento* 4: 23-45
- Bunch, J. N. 1976. D.Phil. thesis. Univ. Oxford. Available from Rutherford Laboratory, *HEP/T/70*
- Camps, C. et al. 1975. *Nucl. Instrum. Methods* 131: 411-16
- Chang, T. N., Fano, U. 1976. *Phys. Rev. A* 13: 263-81
- Charpak, G. 1970. *Ann. Rev. Nucl. Sci.* 20: 195-254
- Chechin, V. A. et al. 1972. *Nucl. Instrum. Methods* 98: 577-87
- Chechin, V. A., Ermilova, V. C. 1976. *Nucl. Instrum. Methods* 136: 551-58
- Cobb, J. H. 1975. D.Phil. thesis. Univ. Oxford. Available from Rutherford Laboratory, *HEP/T/55*
- Cobb, J. H., Allison, W. W. M., Bunch, J. N. 1976. *Nucl. Instrum. Methods* 133: 315-23
- Cobb, J. H. et al. 1977. *Nucl. Instrum. Methods* 140: 413-27
- Commichau, V. et al. 1979. *CERN/EP/EHS/PH79-3*
- Crispin, A., Fowler, G. N. 1970. *Rev. Mod. Phys.* 42: 290-316
- Davidenko, V. A. et al. 1969. *Nucl. Instrum. Methods* 67: 325-30
- Dhawan, S., Ludlam, T. 1978. *IEEE Trans. Nucl. Sci.* NS-25: 944-51
- Dimcovski, Z. et al. 1971. *Nucl. Instrum. Methods* 94: 151-55
- Eckardt, V. et al. 1977. *Nucl. Instrum. Methods* 143: 235-39
- Ermilova, V. C., Kotenko, L. P., Merzon,

- G. I. 1977. *Nucl. Instrum. Methods* 145:555-63
- Fancher, D. et al. 1979. *Nucl. Instrum. Methods* 161:383-90
- Fano, U. 1947. *Phys. Rev.* 72:26-29
- Fano, U. 1963. *Ann. Rev. Nucl. Sci.* 13:1-66
- Fano, U., Cooper, J. W. 1968. *Rev. Mod. Phys.* 40:441-507
- Farr, W. et al. 1978. *Nucl. Instrum. Methods* 156:283-86
- Farr, W., Heintze, J. 1978. *Nucl. Instrum. Methods* 156:301-9
- Fermi, E. 1940. *Phys. Rev.* 57:485-93
- Fischer, J. et al. 1975. *Nucl. Instrum. Methods* 127:525-37
- Fisher, C. M., Guy, J. G., Venus, W. A. 1975. *Nucl. Instrum. Methods* 133:29-34
- Frehe, H. et al. 1978. *Nucl. Instrum. Methods* 156:87-96
- Friedrich, D. et al. 1979. *Nucl. Instrum. Methods* 158:81-88
- Garibyan, G. M. 1960. *Sov. Phys. JETP* 10:372-76
- Garibyan, G. M., Ispiryan, K. A. 1972. *JETP Lett.* 16:413-15
- Gemmell, D. S. 1974. *Rev. Mod. Phys.* 46:129-227
- Harris, F. et al. 1973. *Nucl. Instrum. Methods* 107:413-22
- Hasebe, N. et al. 1978. *Nucl. Instrum. Methods* 155:491-501
- Heintze, J. 1978. *Nucl. Instrum. Methods* 156:227-44
- ICRU. 1979. *Int. Comm. on Radiat. Units Measure. Ave. energy required to produce an ion pair. Rep. 31*
- Inokuti, M. 1971. *Rev. Mod. Phys.* 43:297-347
- Inokuti, M. 1975. *Radiat. Res.* 64:6-22
- Inokuti, M., Itikawa, Y., Turner, J. E. 1978. *Rev. Mod. Phys.* 50:23-35
- Ispiryan, K. A., Margarian, A. T., Zverev, A. M. 1974. *Nucl. Instrum. Methods* 117:125-29
- Jackson, J. D. 1975. *Classical Electrodynamics*, pp. 310-12 New York: Wiley. 848 pp. 2nd ed.
- Jeanne, D. et al. 1973. *Nucl. Instrum. Methods* 111:287-300
- Kopot, E. A. et al. 1976. *Sov. Phys. JETP* 70:387-96; transl. 43:200-4
- Landau, L. 1944. *J. Phys. USSR* 8:201-5
- Landau, L., Lifshitz, E. M. 1960. *Electrodynamics of Continuous Media*, pp. 256-62, 344-59. New York: Pergamon
- Lapique, F., Puiz, F. 1980. *CERN/EF 79-4* (submitted to *Nucl. Instrum. Methods*)
- Lee, L. C. et al. 1973. *J. Quant. Spectrosc. Radiat. Transfer* 13:1023-31
- Lee, L. C. et al. 1977. *J. Chem. Phys.* 67:1237-46
- Lehraus, I. et al. 1978. *Nucl. Instrum. Methods* 153:347-55
- Litt, J., Meunier, R. 1973. *Ann. Rev. Nucl. Sci.* 23:1-43
- Maccabee, H. D., Papworth, D. G. 1969. *Phys. Lett. A* 30:241-42
- Manson, S. T. 1972. *Phys. Rev. A* 5:668-77
- McGuire, E. J. 1968. *Phys. Rev.* 175:20-30
- McGuire, E. J. 1971. *Phys. Rev. A* 3:267-79
- Nygren, D., spokesman. 1976. Proposal for a PEP facility based on the time projection chamber. *PEP-4 proposal*.
- Onuchin, A. P., Telnov, V. I. 1974. *Nucl. Instrum. Methods* 120:365-68
- Pleming, R. W. 1977. D.Phil. thesis. Univ. Oxford. Available from Rutherford Laboratory, *HEP/T/69*
- Ramana Murthy, P. V., Demeester, G. D. 1967. *Nucl. Instrum. Methods* 56:93-105
- Rehak, P., Walenta, A. H. 1980. *IEEE Trans Nucl. Sci.* NS-27:54-58
- Seguinot, J., Ypsilantis, T. 1977. *Nucl. Instrum. Methods* 142:377-91
- Smith, G. C., Mathieson, E. 1975. *Nucl. Instrum. Methods* 131:13-15
- Söchting, K. 1979. *Phys. Rev. A* 20:1359-65
- Srdoc, D. 1973. *Nucl. Instrum. Methods* 108:327-32
- Sternheimer, R. M. 1952. *Phys. Rev.* 88:851-59
- Sternheimer, R. M., Peierls, R. F. 1971. *Phys. Rev. B* 3:3681-92
- Talman, R. 1979. *Nucl. Instrum. Methods* 159:189-211
- Wadsworth, B. F. et al. 1979. *IEEE Trans. Nucl. Sci.* NS-26:120-28
- Wagner, A. et al. 1980. *Nucl. Instrum. Methods*. In press
- Walenta, A. H. et al. 1979. *Nucl. Instrum. Methods* 161:45-58
- Way, K. 1978. *At. Nucl. Data Tables* 22:125-30
- West, J. B., Marr, G. V. 1976. *Proc. R. Soc. Ser. A* 349:397-421; *At. Nucl. Data Tables* 18:497-508
- West, J. B., Morton, J. 1978. *At. Nucl. Data Tables* 22:103-7
- Williams, E. J. 1929. *Proc. R. Soc. Ser. A* 125:420-45